

# Interpretation of global tsunami height distribution due to the 2022 Hunga Tonga-Hunga Ha'apai volcanic eruption

Kei Yamashita (✉ [yamashita\\_kei\\_md8@nra.go.jp](mailto:yamashita_kei_md8@nra.go.jp))

Nuclear Regulation Authority

Taro Kakinuma

Kagoshima University

---

## Article

### Keywords:

**Posted Date:** June 16th, 2022

**DOI:** <https://doi.org/10.21203/rs.3.rs-1761920/v1>

**License:**  This work is licensed under a Creative Commons Attribution 4.0 International License.

[Read Full License](#)

---

1

# Interpretation of global tsunami height distribution due to the 2022 Hunga Tonga-Hunga Ha'apai volcanic eruption

4 Kei Yamashita<sup>a\*</sup> and Taro Kakinuma<sup>b</sup>

<sup>a</sup>Regulatory Standard and Research Department, Nuclear Regulation Authority, Tokyo 106-8450, Japan

<sup>b</sup>Graduate School of Science and Engineering, Kagoshima University, Kagoshima 890-0065, Japan

<sup>7</sup> \*Nuclear Regulation Authority, 1-9-9 Roppongi, Minato-ku, Tokyo 106-8450, Japan;

8 yamashita\_kei\_md8@nra.go.jp

## Abstract

Tsunamis generated by atmospheric pressure waves due to a volcanic eruption were investigated based on both the proposed estimation formulas and numerical calculations. First, assuming linear shallow water conditions, estimation formulas were proposed for the maximum possible amplitude and the resonance distance. Second, the fundamental properties of tsunamis generated by atmospheric pressure waves were examined numerically using both the nondispersion and weak dispersion models. Based on the numerical results, a ridge and shelf can amplify tsunamis due to atmospheric pressure waves beyond the limits of the Proudman resonance. The estimated and numerically determined maximum possible amplitudes agreed well when the dispersion of tsunamis was not large. Third, the distribution maps of the maximum possible amplitude and the resonance distance for various traveling velocities of atmospheric pressure waves were generated using the proposed formulas. The maximum tsunami amplitude depends on both the length of the excitation area and the resonance distance along the path of atmospheric pressure waves. The worldwide distribution of both the tsunami height and the appearance time of the maximum tide level fluctuations due to the 2022 Tonga volcanic eruption and several historical eruptions were interpreted based on the distribution maps. In the historical large eruptions, the period of the atmospheric pressure waves was shorter; thus, the dispersion effect was larger, resulting in a smaller tsunami amplitude.

## Introduction

Due to the large eruption of the 2022 Hunga Tonga-Hunga Ha'apai volcano at around 13:00 on January 15, 2022 (JST), tsunamis were observed off the Pacific coast (Japan Standard Time (JST), UTC + 9 h, is used in this paper). The tsunamis with a height of around 1.5 m struck the capital Nuku'alofa of Tonga, 65 km away from the volcano, whereafter they attenuated to several tens of centimeters at the coasts of the neighboring countries<sup>1</sup>. Conversely, the tsunamis with a height of >1 m reached the coasts of the Pacific Rim countries far from Tonga, including New Zealand, Australia, Japan, Northern Alaska, Northern California, and Chile. For example, at Amami, Japan, large tide level fluctuations started at around 23:35, and the maximum total amplitude was >2.5 m<sup>1</sup>. Near the eruption site, the large attenuation of tsunamis was observed as in the tsunamis caused by a mountain collapse, landslide, and surge intrusion. Conversely, far from the eruption site, tsunamis with different properties were observed. For example, large tide level fluctuations started 55 min earlier than the predicted time of the tsunamis generated at the eruption site to arrive at Amami. Prior to this large fluctuations, abnormal tide level fluctuations started at around 20:50 in Amami, following the atmospheric pressure waves, which showed the peak value of atmospheric pressure deviation at 20:40 at Amami, based on the data obtained by Weathernews meteorological observer "Soratena." The atmospheric pressure waves were observed all over Japan. On Chichijima Island, Japan, after the atmospheric pressure deviation showed the peak value at around 19:00, the abnormal tide level fluctuations started at 19:58, and the maximum tsunami height appeared at 22:52<sup>1</sup>. Moreover, tsunamis were observed across islands and lands, including the Caribbean Sea, Indian Ocean, and Atlantic Ocean<sup>2</sup>.

The atmospheric pressure waves originating from the large eruption of Krakatau in 1883 excited the abnormal tide level fluctuations at the coasts of Australia, the United States, South Africa, and the United Kingdom, far from the volcano<sup>3</sup>. However, the maximum amplitude of the tsunamis was approximately 0.3 m at most<sup>4</sup>. Regarding the 1991 Pinatubo volcanic eruption, although the volcanic eruption index (VEI) was 6, which is equal to or greater than that of the 2022 Hunga Tonga-Hunga Ha'apai volcanic eruption, tsunamis amplified to 1 m or more by atmospheric pressure waves were not reported. It has not been revealed why these large-scale volcanic eruptions did not cause large tsunamis.

Recently established atmospheric pressure observations suggested that the atmospheric pressure vibrations due to the 2022 Hunga Tonga-Hunga Ha'apai volcanic eruption, which is referred to as the 2022 Tonga eruption hereinafter, included different components such as the atmospheric Lamb waves, sound waves, and atmospheric gravity waves<sup>1</sup>. Based on both the tide gauge records and atmospheric pressure data, the relationship between the tsunamis and the atmospheric Lamb wave with the largest atmospheric pressure deviation, which was 2 hPa in Japan, has been numerically investigated. For example, tsunamis due to a pulsed atmospheric Lamb wave were simulated on a global scale using the linear shallow water model<sup>5</sup>. A pulsed atmospheric Lamb wave was idealized and one-dimensional nonlinear shallow water waves were calculated over model seabed topographies<sup>6,7</sup>. These studies indicated that the atmospheric Lamb wave can explain the initial time of the observed tide level fluctuations. Conversely, it was suggested that the atmospheric gravity

waves at a traveling velocity of 200–250 m/s, following the pulsed atmospheric Lamb wave, could cause an effective Proudman resonance<sup>8</sup> in the areas of the Pacific Ocean with a water depth of 4000–5000 km, leading to large tide level fluctuations<sup>5</sup>. Moreover, the relationship between the atmospheric pressure spectra and bay water oscillations was examined<sup>9</sup>. Tsunamis with a height of 2 m were reported in Ensenada, Baja California and Manzanillo, Colima, Mexico<sup>10</sup>. However, the amplification mechanism of tsunamis with a total amplitude of over 1 m is still unknown, and the global tsunami height distribution has not been analyzed.

In this work, we interpret the global tsunami height distribution due to the 2022 Tonga eruption. We first propose the estimation formulas for the maximum possible amplitude and resonance distance of tsunamis due to an atmospheric pressure wave. Second, we perform the verification of the estimation formulas for the maximum possible amplitude based on the one-dimensional numerical simulations of tsunamis using a pressure wave model. The effects of a ridge and shelf on the propagation processes of tsunamis due to atmospheric pressure waves are also evaluated numerically by simulating the tsunamis. Third, we interpret the global tsunami height distribution due to the 2022 Tonga eruption, based on the distributions of the maximum possible amplitude and resonance distance of tsunamis obtained using the estimation formulas. Finally, we summarize the tsunamis caused by atmospheric pressure waves due to several large historical eruptions.

## Results and discussion

### ***Verification of the estimation formula for the maximum possible amplitude of tsunamis due to atmospheric pressure waves***

The proposed estimation formulas for the maximum possible amplitude  $H_{\max}$  and the maximum possible wavelength  $L_{\max}$  of tsunamis due to an atmospheric pressure wave are as follows:

$$H_{\max} = \frac{a}{\rho g} \left( 2 \left| 1 - \frac{\sqrt{gh}}{v_a} \right| \right)^{-1}, \quad (\text{R1})$$

$$L_{\max} = L_a, \quad (\text{R2})$$

where  $a$  (Pa) is the maximum absolute value of the atmospheric pressure wave,  $\rho$  is the water density,  $g$  is the gravitational acceleration, namely 9.8 m/s<sup>2</sup>,  $h$  is the still water depth,  $v_a$  is the traveling velocity of the atmospheric pressure wave, and  $L_a$  is the wavelength of the atmospheric pressure wave. These equations were derived as Eqs. (M8) and (M9) in **Methods**.

We first verified Eq. (R1) numerically by simulating one-dimensional wave propagation. The calculation region was  $-2000 \text{ km} \leq x \leq 8000 \text{ km}$ , and the still water depth  $h$  was 5500 m, which was the representative water depth in the Pacific Ocean near Japan. The peak location of the triangular pressure distribution  $p(x, t)$  was  $x_p(t) = v_a t$ , where the initial location was  $x_p(0 \text{ s}) = 0 \text{ km}$ . The initial water surface displacement was  $\eta(x, 0 \text{ s}) = -p(x, 0 \text{ s})/\rho g$ , to balance the pressure and water surface profile, where the water density  $\rho$  was 1000 kg/m<sup>3</sup>. The pulses moved at a constant traveling velocity of  $v_a$  at  $0 \text{ min} \leq t \leq 200 \text{ min}$ , and they stopped traveling at  $t = 200 \text{ min}$ .

When an atmospheric pressure wave is traveling, the resonant water wave with a positive amplitude overlaps with the forced water wave with a negative amplitude under the atmospheric pressure wave; thus, the apparent tsunami amplitude is smaller than the corresponding tsunami amplitude evaluated by Eq. (R1). However, after the atmospheric pressure wave stops, the free wave is away from the forced wave under the atmospheric pressure wave; therefore, the tsunami amplitude of the free wave can be compared with the maximum possible amplitude  $H_{\max}$  using Eq. (R1).

The conditions of the atmospheric pressure waves are listed in Tab. 1, where the quantities were determined with reference to the observed atmospheric pressure wave data shown in Fig. 7 in **Method**. The tsunami grows only when it overlaps with the atmospheric pressure wave; thus, the maximum tsunami amplitude depends on the resonance time  $\tau_{\max}$  during which they overlap. The time  $\tau_{\max}$  can be evaluated by Eq. (M6) in **Method**. In Case 5, the actual resonance time  $\tau$  was equal to the traveling time of the atmospheric pressure wave, because the traveling time of the atmospheric pressure wave was shorter than the resonance time  $\tau_{\max}$ . In such cases, the present estimation formulas can also be applied.

**Tab. 1.** Conditions of atmospheric pressure waves.

| Case | Phase Velocity<br>$v_a$ | Maximum<br>Pressure $a$ | Wave Period<br>$T_a$ | Tsunami Amplitude<br>Amplification Factor $\alpha$ | Actual Resonance<br>Time $\tau$ | Maximum Possible<br>Amplitude $H_{\max}$ |
|------|-------------------------|-------------------------|----------------------|--|---------------------------------|--|
| 1    | 300 m/s                 | 2 hPa                   | 30 min               | $1.13 \times 10^{-5}$ m/s                          | 3980 s                          | 0.045 m                                  |
| 2    | 300 m/s                 | 0.5 hPa                 | 5 min                | $1.70 \times 10^{-5}$ m/s                          | 663 s                           | 0.011 m                                  |
| 3    | 250 m/s                 | 0.5 hPa                 | 5 min                | $1.70 \times 10^{-5}$ m/s                          | 2102 s                          | 0.036 m                                  |
| 4    | 250 m/s                 | 0.5 hPa                 | 2 min                | $4.25 \times 10^{-5}$ m/s                          | 841 s                           | 0.036 m                                  |
| 5    | 250 m/s                 | 0.5 hPa                 | 60 min               | $1.42 \times 10^{-6}$ m/s                          | 12,000 s *                      | 0.017 m                                  |
| 6    | 200 m/s                 | 2 hPa                   | 30 min               | $1.13 \times 10^{-5}$ m/s                          | 5596 s                          | 0.063 m                                  |

\* The travel time of the atmospheric pressure wave, i.e., 12,000 s, was shorter than  $\tau_{\max} = 25,230$  s evaluated by Eq. (M6).

Figure 1a shows the time variations of the water surface profiles due to the atmospheric pressure waves in Cases 1, 3, and 6, obtained using both the nondispersion and weak dispersion models. As shown in Fig. 1a, in Case 1, there was almost no difference between the results of the nondispersion and weak dispersion models. The tsunami amplitude was amplified until  $t = 60$  to 75 min, which was close to the resonance time  $\tau_{\max}$ , and consequently, the tsunami amplitude remained constant until the atmospheric pressure wave stopped traveling. The preceding tsunami propagated under the atmospheric pressure wave, whereas the subsequent tsunami propagated at a constant phase velocity of  $\sqrt{gh}$ . After the atmospheric pressure wave stopped traveling, the preceding tsunami was away from the atmospheric pressure wave, with a slightly increased amplitude, and the phase velocity changed from  $v_a$  to  $\sqrt{gh}$ .

In Case 3, the ratio of the water depth to the wavelength of the tsunami was larger than that in Case 1; thus, the tsunami amplitude obtained using the weak dispersion model was less than that obtained using the nondispersion model. After the tsunami amplitude reaches the maximum possible amplitude  $H_{\max}$ , it remains

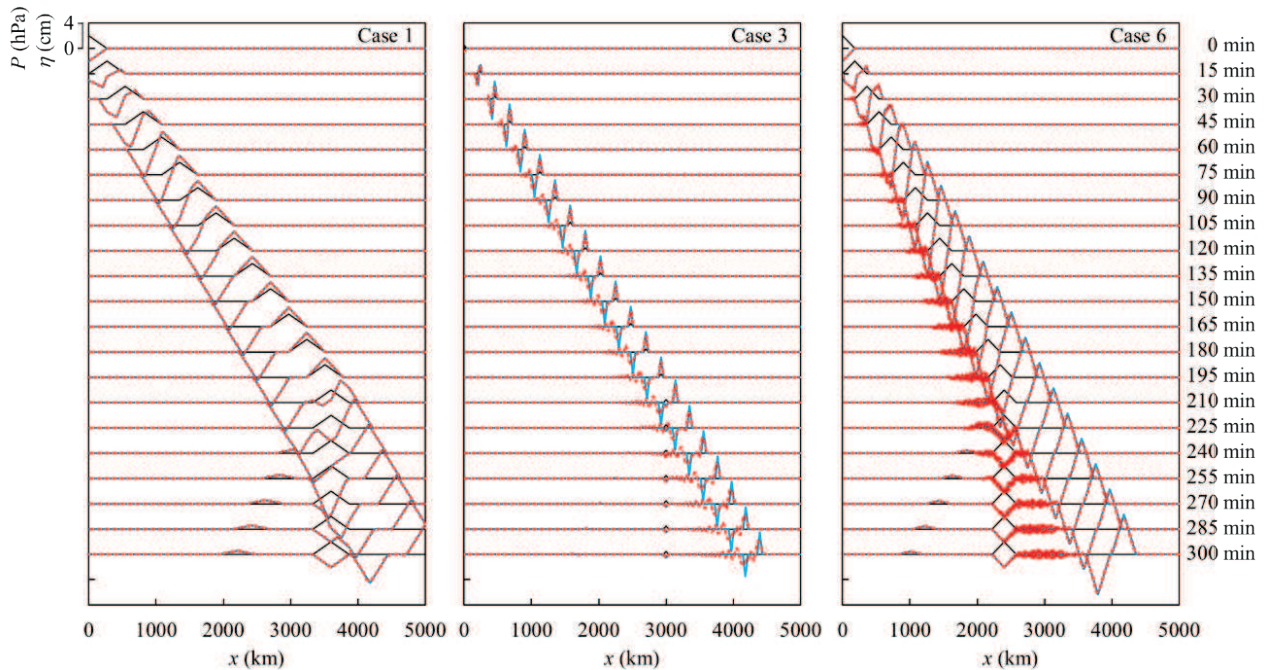
constant under the influence of atmospheric pressure waves, but once the tsunamis move away from the influence of atmospheric pressure waves, the tsunami amplitude is attenuated by wave dispersion in propagation. When the dispersion effect is large, the tsunami amplitude may be overestimated by the estimation formulas, but it can provide useful information for evacuation against tsunamis on the safe side immediately after an eruption when the atmospheric pressure waves are uncertain.

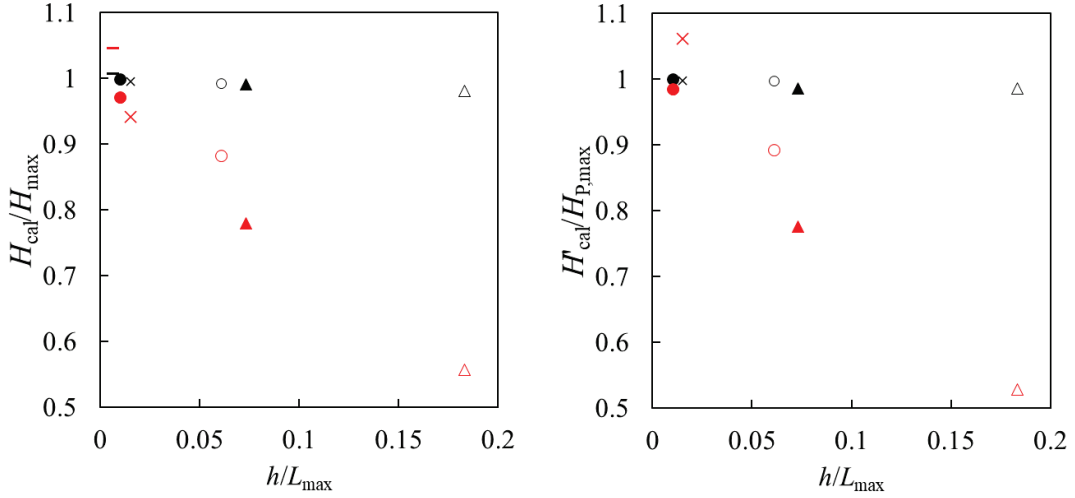
In Case 6, where  $v_a < \sqrt{gh}$ , the preceding water wave propagated at a phase velocity of  $\sqrt{gh}$ , and the subsequent water wave propagated under the atmospheric pressure wave. The tsunami height from the dispersion model was slightly smaller than that obtained using the nondispersion model.

Figure 1b depicts the relationship between the maximum amplitude ratio and the ratio of the still water depth  $h$  to the maximum possible wavelength  $L_{\max}$ , where  $H_{\text{cal}}$  and  $H'_{\text{cal}}$  are the maximum amplitude of tsunamis after and before leaving the influence of atmospheric pressure waves, respectively, obtained by numerical calculations, and  $H_{\max}$  and  $H_{P,\max}$  are the maximum possible amplitudes of tsunamis away from and under the influence of the atmospheric pressure wave, respectively, where  $H_{\max}$  and  $H_{P,\max}$  can be estimated using Eq. (R1) and Eq. (M1) in **Methods**, respectively.

As indicated in Fig. 1b, the estimated values of  $H_{\max}$  and  $H_{P,\max}$  under the shallow water assumption were in harmony with the calculated values obtained using the nondispersion model. However, when  $h/L_{\max}$  was large, the estimated values were larger than the corresponding calculated values obtained using the weak dispersion model. Thus, the actual tsunami height is smaller than the estimated value in a deeper water area when the wavelength of an atmospheric pressure wave is shorter because the maximum wavelength of the resonant wave depends on the wavelength of the atmospheric pressure wave.

**Fig. 1: Verification of the estimation formulas.**





150

**b**

151 **a** Time variations of water surface profiles due to the atmospheric pressure waves in Cases 1, 3, and 6, the  
 152 conditions of which are described in Tab. 1. The black line indicates the atmospheric pressure  $p$ . The blue and  
 153 red lines indicate the water surface displacements  $\eta$ , obtained using the nondispersion and weak dispersion  
 154 models, respectively. **b** Relationship between the maximum amplitude ratio and the ratio of the still water  
 155 depth  $h$  to the maximum possible wavelength  $L_{\text{max}}$ , where  $H_{\text{cal}}$  and  $H'_{\text{cal}}$  are the maximum amplitudes of the  
 156 tsunamis after and before leaving the influence of the atmospheric pressure wave, respectively, obtained by  
 157 numerical calculations, and  $H_{\text{max}}$  and  $H_{p,\text{max}}$  are the maximum possible amplitudes estimated using Eqs. (R1)  
 158 and (M1), respectively. The black and red plots indicate the results obtained using the nondispersion and weak  
 159 dispersion models, respectively. The marks  $\bullet$ ,  $\circ$ ,  $\blacktriangle$ ,  $\triangle$ ,  $-$ , and  $\times$  denote the results for Cases 1, 2, 3, 4, 5,  
 160 and 6, respectively.

161

162 We investigated the effects of the ridge and shelf topographies between Tonga and Japan on tsunami  
 163 propagation due to atmospheric pressure waves. Tsunamis caused by atmospheric pressure waves due to an  
 164 eruption over seabed topography were theoretically and numerically investigated<sup>11,12</sup>. The seabed topography  
 165 is depicted in Fig. 2a.

166 The profiles of the atmospheric pressure waves were given by

167 
$$p(x, t) = 0.5a [1.0 + \cos(kx - \sigma t)] \quad \text{for } x_a - 0.5L_a - (n-1)L_a < x < 0.5L_a + x_a, \quad (\text{R3})$$

168 where the wave number and angular frequency are denoted by  $k = 2\pi/L_a$  and  $\sigma = 2\pi/T_a$ , respectively. The  
 169 location of the peak of the first atmospheric pressure wave was  $x_a(t) = v_a \cdot t = (\sigma/k) \cdot t$ .

170 When the number of the atmospheric pressure waves,  $n$ , is 10, the time variations of water surface profiles  
 171 are presented in Fig. 2b, where  $a = 0.5$  hPa,  $v_a = 250$  m/s,  $L_a = 75,000$  m, and  $T_a = 300$  s. Figure 2c depicts the  
 172 maximum water level distributions, when  $n$  is 1 or 10.

173 First, regarding the results obtained using the nondispersion model, when the atmospheric pressure waves  
 174 travel over the uniform still water depth, a wave group of tsunamis with the maximum possible amplitude  $H_{\text{max}}$   
 175 of approximately 0.36 m are generated, indicating beating water level fluctuations with both nodes and

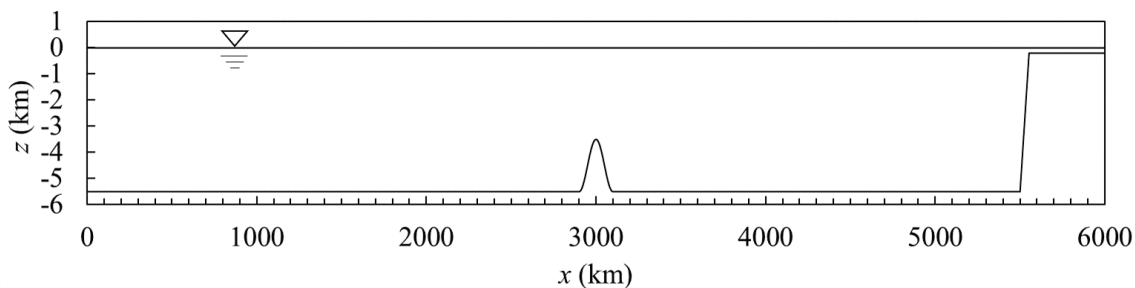
176 antinodes. For example, a node is formed at  $x \approx 1200$  km and 1900 km.

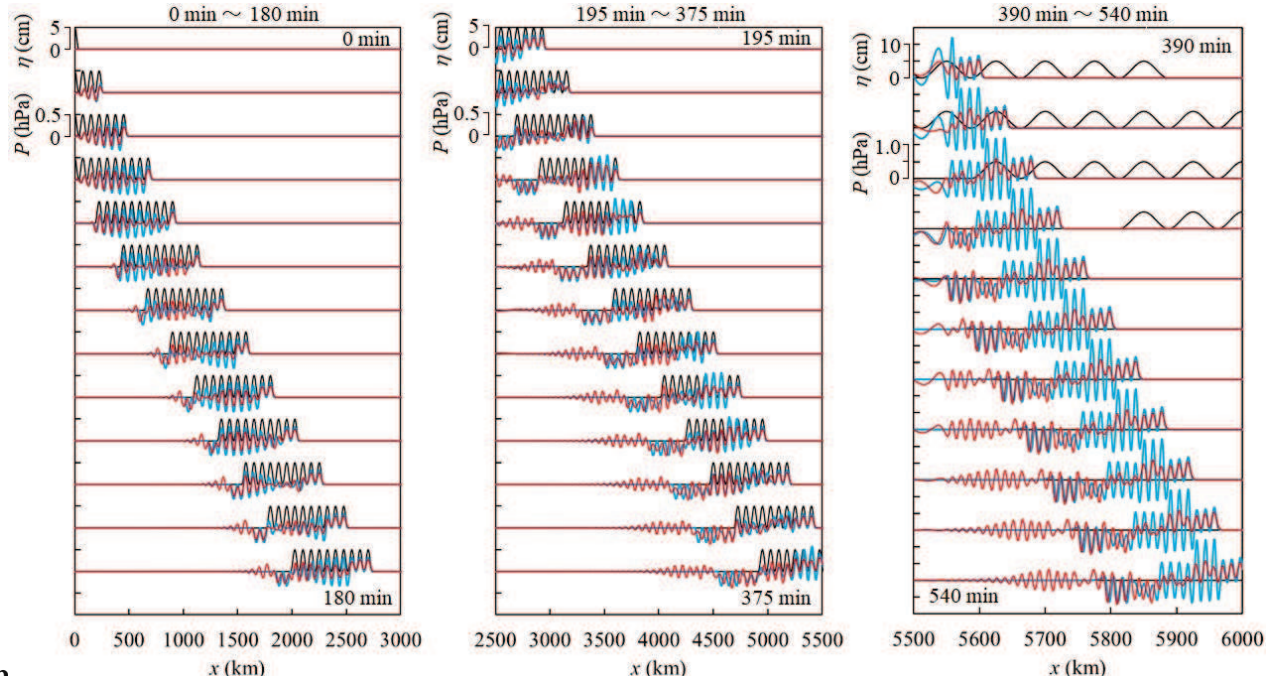
177 Second, after the wave group passes through the ridge, the tsunamis that followed the atmospheric  
178 pressure waves like forced waves leave the influence of the atmospheric pressure waves, changing the phase  
179 velocity instantly from  $v_a$  to  $\sqrt{gh}$ . Later, the atmospheric pressure waves that leave the tsunamis start to  
180 generate new tsunamis; therefore, the number of tsunamis increases even without wave disintegration.  
181 Therefore, the new wave group behind the ridge is composed of two types of resonant waves with different  
182 phase velocities, resulting in beating in which the subsequent tsunami amplitudes increase and decrease  
183 periodically. The tsunami amplitude is amplified to approximately twice as much as  $H_{\max}$  by the  
184 superimposition of the water wave propagating as free waves with a phase velocity of  $\sqrt{gh}$  and new water  
185 wave generated behind the ridge with a phase velocity of  $v_a$ .

186 Third, when this beating wave group reaches the shelf slope, the atmospheric pressure waves instantly  
187 leave the tsunamis, and the phase velocity of all the components of tsunamis becomes  $\sqrt{gh}$ , stopping periodic  
188 beating. Therefore, depending on the timing of beating when passing through the shelf slope, tsunamis with an  
189 amplitude larger than  $H_{\max}$  are incident on the shelf, even without amplification due to shallowing over the  
190 shelf slope.

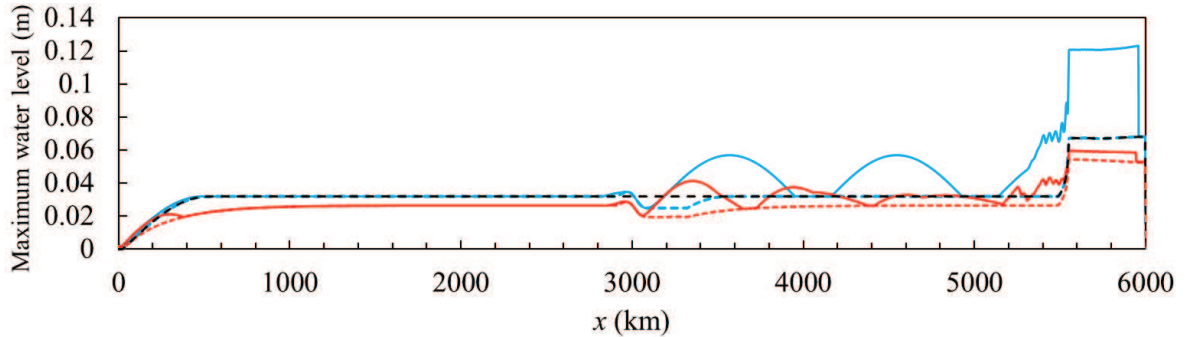
191 Conversely, regarding the results obtained using the weak dispersion model, although the amplitude of  
192 the tsunamis generated and amplified by multiple atmospheric pressure waves is spatially periodic and  
193 increases by passing through the changes in the water depth, the tsunami amplitude is smaller than that  
194 calculated using the nondispersion model. As the wavelength or period of atmospheric pressure waves  
195 decreases, the wave dispersion becomes more effective, and the tsunami amplitude decreases. Thus, the  
196 influence of the shorter-period components of atmospheric pressure waves with much dispersion of tsunamis  
197 is relatively smaller on the amplification of tsunamis.

198  
199 **Fig. 2: Propagation of tsunamis due to atmospheric pressure waves over a ridge and shelf.**





201      b



202      c

203    **a** Seabed topography including a ridge and shelf, where the largest water depth  $h$  was 5500 m. The ridge height  
 204    was 2000 m and the ridge width was 200 km. The shelf-slope width was 50 km and the water depth over the  
 205    shelf was 200 m. **b** Time variations of water surface profiles every 15 min. The black line indicates the  
 206    atmospheric pressure  $p$ . The blue and red lines indicate the water surface displacements  $\eta$ , obtained using the  
 207    nondispersion and weak dispersion models, respectively. **c** Distributions of the maximum water levels. The  
 208    blue and red lines indicate the results calculated using the nondispersion and weak dispersion models. The  
 209    broken and solid lines indicate the results when the number of the atmospheric pressure waves,  $n$ , is 1 and 10,  
 210    respectively. The broken black line indicates the result without the ridge when  $n$  is 1, calculated using the  
 211    nondispersion model.

212

213    ***Interpretation of the global tsunami height distribution 1: Distributions of the maximum possible amplitude***  
 214    ***for various traveling velocities of atmospheric pressure waves***

215    Figure 3a summarizes the maximum total amplitudes in the tide level fluctuations at various locations

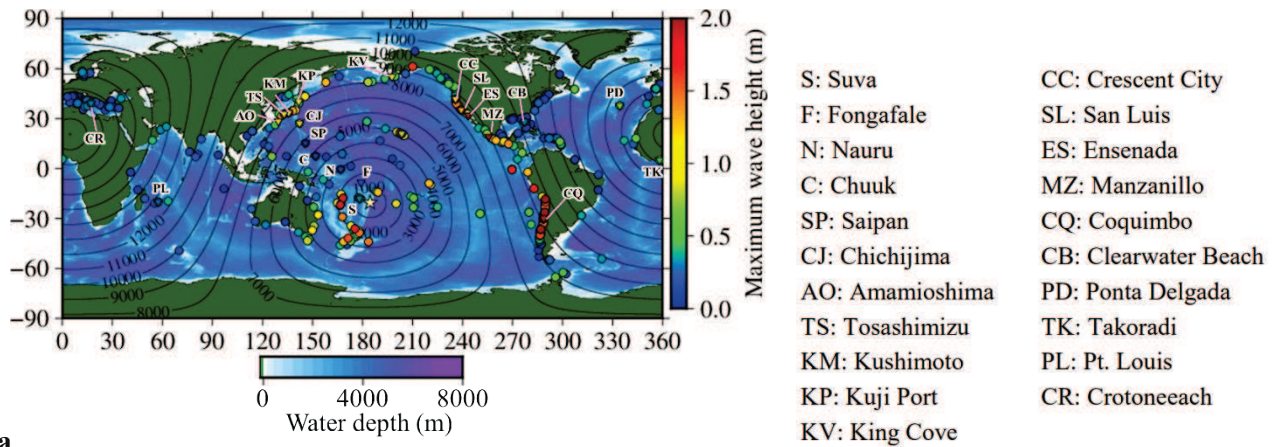
216 pointed with circles<sup>2</sup>. The color map presents the bathymetry of GEBCO. The mark  $\star$  indicates the site of the  
 217 2022 Tonga eruption, the distance from which is indicated by isolines every 1000 km.

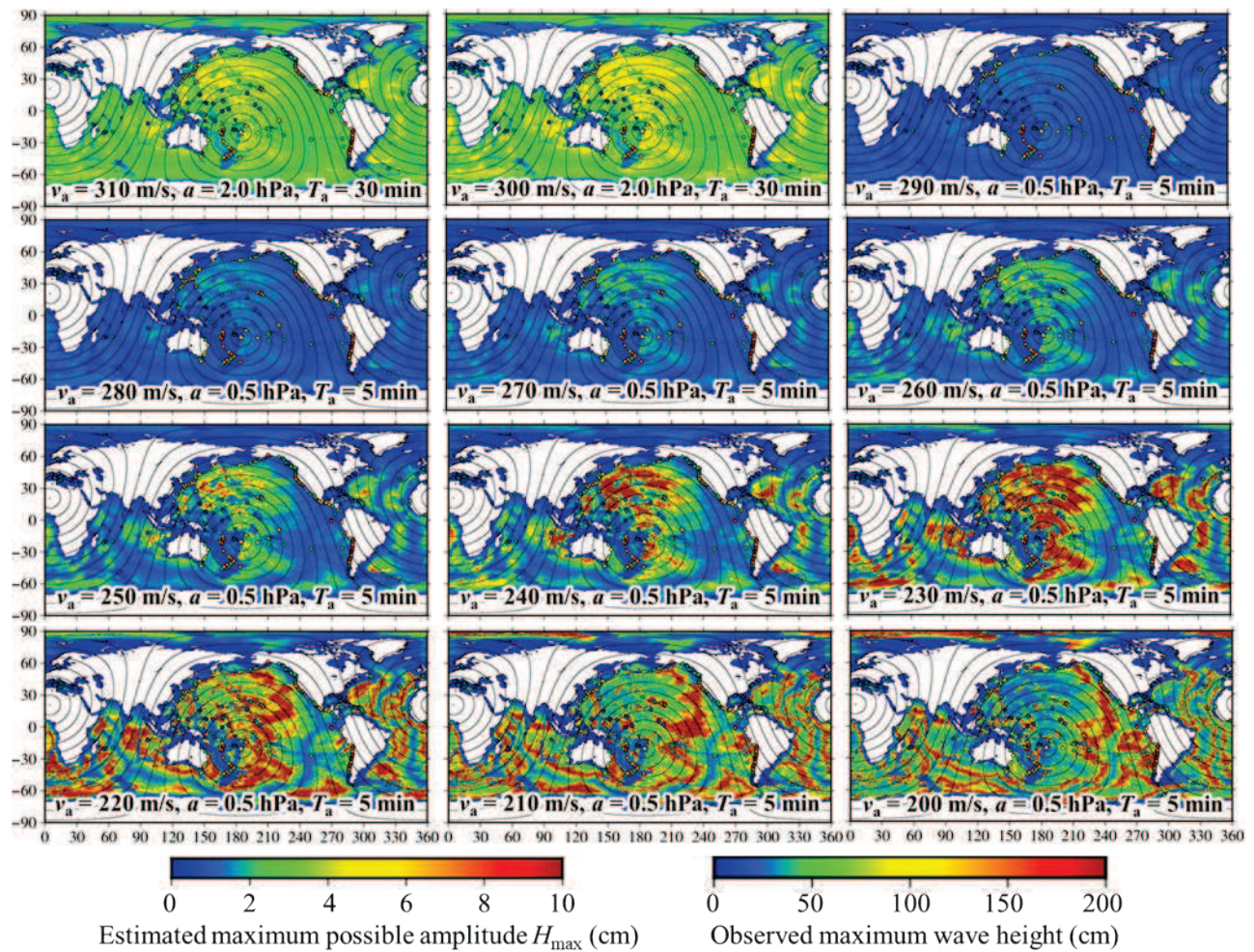
218 Using the seawater depth  $h$  depicted in Fig. 3a, the distributions of the maximum possible amplitude  $H_{\max}$   
 219 based on Eq. (R1) in which the seawater density  $\rho$  was assumed to be  $1020 \text{ kg/m}^3$  are shown in Fig. 3b for  
 220 various traveling velocities of atmospheric pressure waves. Although the regional difference in the period of  
 221 atmospheric pressure waves is not large, that in the pressure deviation is large: assuming that the atmospheric  
 222 pressure waves propagate concentrically, the pressure deviation is larger near the eruption site, decreases in,  
 223 e.g., Japan located approximately 1/4 of the circumference of Earth, and beyond Japan, converges and grows  
 224 larger. In the present study, avoiding overestimation, we used the representative values of the atmospheric  
 225 pressure waves following the Lamb wave in Japan,  $a$  was  $0.5 \text{ hPa}$  and  $T_a$  was  $5 \text{ min}$ . The isolines indicate the  
 226 distance from the site of the 2022 Tonga eruption every 1000 km. The maximum possible amplitude is larger  
 227 in deeper water areas with a water depth  $h$  in the range of  $2000\text{--}9000 \text{ m}$ , indicating that the tsunami amplitude  
 228 in coastal regions with  $h$  of  $5 \text{ m}$  is  $4.5\text{--}6.5$  times based on the Green law.  
 229

230 ***Interpretation of the global tsunami height distribution 2: Distributions of resonance distance for various***  
 231 ***traveling velocities of atmospheric pressure waves***

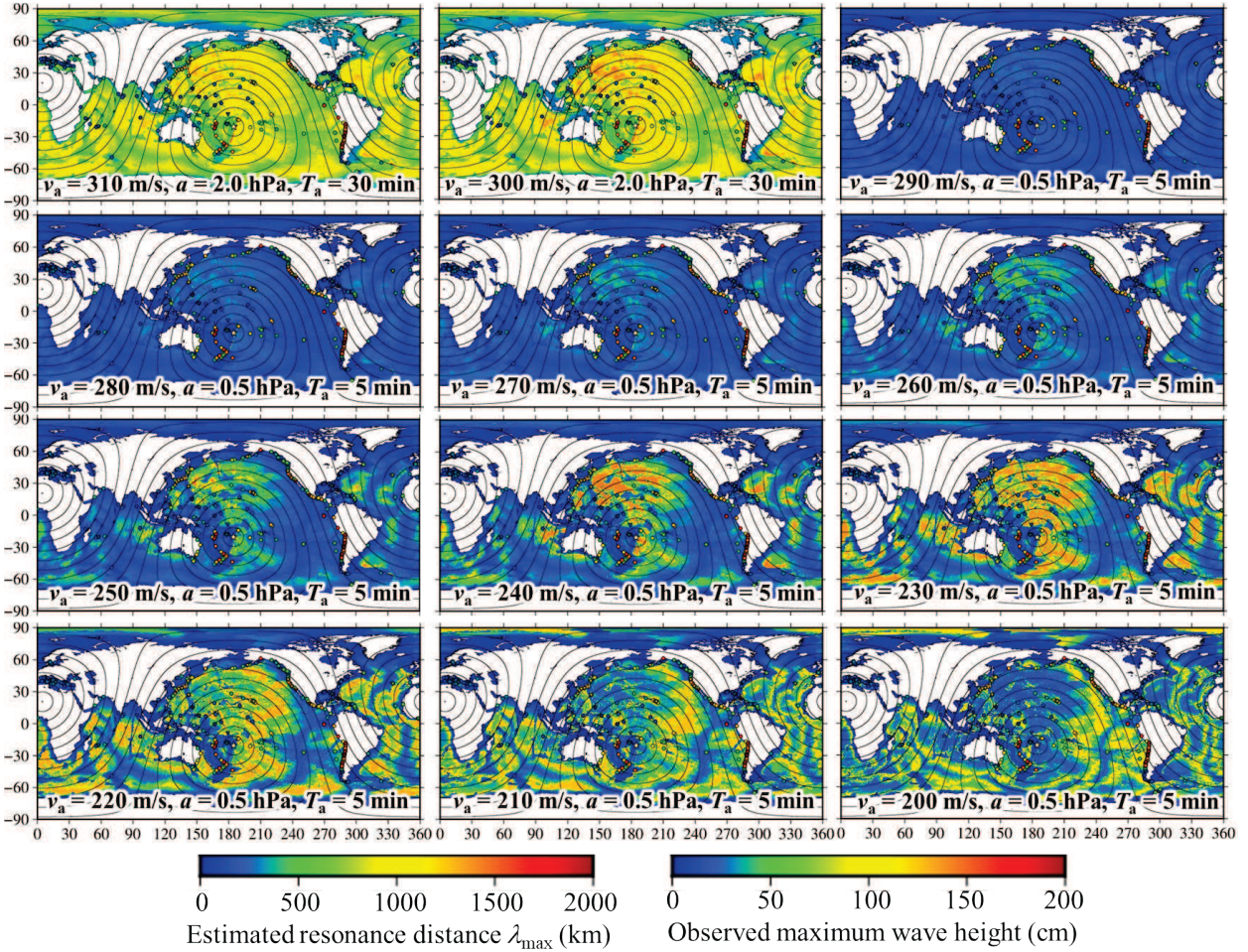
232 Figure 3c depicts the resonance distance  $\lambda_{\max}$  based on Eq. (M7) in **Methods** for various traveling  
 233 velocities of atmospheric pressure waves. The isolines indicate the distance from the site of the 2022 Tonga  
 234 eruption at every 1000 km. The resonance distance  $\lambda_{\max}$  indicates whether the maximum possible amplitude  
 235  $H_{\max}$  presented in Fig. 3b can be achieved or not.  
 236

237 **Fig. 3: Global estimation of tsunamis excited by atmospheric pressure waves.**





240



241

**c**

242 **a** Maximum total amplitudes of the tide level fluctuations at various locations pointed by circles<sup>2</sup>. The color  
 243 map presents the bathymetry of GEBCO. The color of the marks  $\nabla$  indicates the maximum tsunami height  
 244 from the observed data of UNESCO/IOC. The mark  $\star$  indicates the site of the 2022 Tonga eruption, the  
 245 distance from which is indicated by isolines every 1000 km. **b** Distributions of the maximum possible  
 246 amplitude  $H_{\max}$  predicted using Eq. (M8) for various traveling velocities of atmospheric pressure waves, where  
 247 the upper limit of the maximum possible amplitude was 0.1 m. The maximum absolute value of the  
 248 atmospheric pressure,  $a$ , and the period of the pulse,  $T_a$ , were 0.5 hPa and 5 min, respectively. The seawater  
 249 density  $\rho$  was assumed to be 1020 kg/m<sup>3</sup>. The maximum total amplitudes of tide level fluctuations<sup>2</sup> depicted  
 250 in Fig. 3a are also indicated at the locations pointed with circles. The isolines indicate the distance from the  
 251 site of the 2022 Tonga eruption every 1000 km. **c** Distributions of resonance distance  $\lambda_{\max}$  predicted using Eq.  
 252 (M7) for various traveling velocities of atmospheric pressure waves, where the upper limit of the maximum  
 253 possible amplitude was 0.1 m. The maximum absolute value of the atmospheric pressure,  $a$ , and the period of  
 254 the pulse,  $T_a$ , were 0.5 hPa and 5 min, respectively. The isolines indicate the distance from the site of the 2022  
 255 Tonga eruption every 1000 km. The maximum total amplitudes of tide level fluctuations<sup>2</sup> depicted in Fig. 3a  
 256 are also indicated at the locations pointed by circles.

257

258    ***Interpretation of the global tsunami height distribution 3: Global tsunami height distribution caused by***  
 259    ***atmospheric pressure waves due to the 2022 Tonga eruption***

260    We consider the global tsunami height distribution based on both  $H_{\max}$  and  $\lambda_{\max}$  shown in Figs. 3b and 3c,  
 261    respectively. Specifically, the tsunamis in each area were as follows:

262    (1) Pacific islands

263    The observed tide level fluctuations in the island regions, namely Fiji-Suva, Tuvalu-Fongafale, Nauru,  
 264    Micronesia-Chuuk, Mariana Islands, and Saipan, located 700–5820 km northwest of Tonga were relatively  
 265    small in range of 0.1–0.3 m, as indicated in Fig. 3b and Tab. 2. Although Fig. 3b. indicates that significant  
 266    tsunamis were not generated at the coasts of the neighboring countries west to south of Tonga, larger tsunamis  
 267    were observed at these locations, so the tsunamis could reach these coasts from the eruption site, with a strong  
 268    directivity.

269  
 270    **Tab. 2. Estimated arrival time  $t_{\text{tsunami}}$  at each tsunami observation location, where the values of  $t_{\text{tsunami}}$**   
 271    **calculated by Eq. (M15) are shown in red, for the 2022 Tonga eruption.** The estimated arrival time  $t_{\text{air}}$   
 272    evaluated by Eq. (M17) for each traveling velocity of atmospheric pressure waves,  $v_a$ , is shown in blue. The  
 273    mean value of the still water depth  $h$  was determined according to Eq. (M16). “NA” means that the data were  
 274    not available, and “NC” means that the data were not clear. The table was created using the data of NOAA,  
 275    Study session on tsunami prediction technology<sup>1</sup>, Ramírez-Herrera et al.<sup>10</sup>, and UNESCO/IOC<sup>13</sup>.

| Country/Region                       | Distance from the Eruption Site (km) | Observed Maximum Tsunami Height (m) | Elapsed Time from the Eruption (h) |  |   | Traveling Velocity of Atmospheric pressure Waves, $v_a$ (m/s) |      |      |      |      |      |         |
|--------------------------------------|--------------------------------------|-------------------------------------|------------------------------------|--|---|---|------|------|------|------|------|---------|
|                                      |                                      |                                     | Start of Tide Level Fluctuations   | Start of Maximum Tide Level Fluctuations | Appearance of Maximum Tide Level Fluctuations | 300   | 250  | 240  | 230  | 220  | 210  | 200     |
| Suva, Fiji                           | 730                                  | 0.3                                 | 1.0                                | NC                                       | 1.8   | 0.7   | 0.8  | 0.8  | 0.9  | 0.9  | 1.0  | 1.0     |
| Fongafale, Tuvalu                    | 1460                                 | 0.2                                 | 2.0                                | NC                                       | 3.3   | 1.4   | 1.3  | 1.7  | 1.8  | 1.8  | 1.9  | 2.0     |
| Nauru, Nauru                         | 2940                                 | 0.1                                 | 3.4                                | NC                                       | 7.3   | 2.7   | 3.3  | 3.4  | 3.6  | 3.7  | 3.9  | 4.1     |
| Chuuk, Micronesia                    | 4750                                 | 0.1                                 | 5.0                                | NC                                       | 17.5  | 4.4   | 5.3  | 5.5  | 5.7  | 6.0  | 6.3  | 6.6     |
| Saipan, the USA                      | 5820                                 | < 0.1                               | 5.8                                | NC                                       | NC  | 5.4   | 6.5  | 6.7  | 7.0  | 7.4  | 7.7  | 8.1     |
| Kahului, Hawaii, the USA             | 5050                                 | 0.8                                 | 5.3                                | 6.5–7.5                                  | 8.4   | 4.7   | 5.6  | 5.8  | 6.1  | 6.4  | 6.7  | 7.0     |
|                                      |                                      |                                     |                                    |  |   |   |      |      |      |      |      | 6.6     |
| San Luis, California, the USA        | 8470                                 | 1.3                                 | 7.8                                | 11.8                                     | 13  | 7.8   | 9.4  | 9.8  | 10.2 | 10.7 | 11.2 | 11.8    |
| Crescent City, California, the USA   | 8710                                 | 1.1                                 | 8.3                                | 12.0                                     | 14.5  | 8.1   | 9.7  | 10.0 | 10.5 | 11.0 | 11.5 | 12.0    |
|                                      |                                      |                                     |                                    |  |   |   |      |      |      |      |      | 11.3    |
| King Cove, Alaska, the USA           | 8510                                 | 1.0                                 | 9.3                                | 11.4                                     | 12.2  | 7.9   | 9.5  | 9.8  | 10.3 | 10.7 | 11.3 | 11.8    |
|                                      |                                      |                                     |                                    |  |   |   |      |      |      |      |      | 11.0    |
| Coquimbo, Chile                      | 10,160                               | 1.9                                 | 9.5                                | 14–15                                    | 17.4  | 9.4   | 11.3 | 11.8 | 12.3 | 12.8 | 13.4 | 14.1    |
|                                      |                                      |                                     |                                    |  |   |   |      |      |      |      |      | 14.2    |
| Ensenada, Mexico                     | 8560                                 | 2.0                                 | NA                                 | NA                                       | NA  | 7.9   | 9.5  | 9.9  | 10.3 | 10.8 | 11.3 | 11.9    |
|                                      |                                      |                                     |                                    |  |   |   |      |      |      |      |      | 11.7    |
| Manzanillo, Mexico                   | 8910                                 | 2.0                                 | NA                                 | NA                                       | NA  | 8.3   | 9.9  | 10.3 | 10.8 | 11.3 | 11.8 | 12.4    |
|                                      |                                      |                                     |                                    |  |   |   |      |      |      |      |      | 12.2    |
| Chichijima, Ogasawara Islands, Japan | 7000                                 | 0.9                                 | 6.7                                | 9.0                                      | 9.6   | 6.5   | 7.8  | 8.1  | 8.5  | 8.8  | 9.3  | 9.8     |
|                                      |                                      |                                     |                                    |  |   |   |      |      |      |      |      | 8.6–8.8 |
| Kuji Port, Tohoku, Japan             | 8090                                 | 1.1                                 | NA                                 | NA                                       | NA  | 7.5   | 9.0  | 9.4  | 9.8  | 10.2 | 10.7 | 11.2    |
|                                      |                                      |                                     |                                    |  |   |   |      |      |      |      |      | 10.2    |

|  |        |     |     |      |      |      |      |      |      |      |      |      |
|--|--------|-----|-----|------|------|------|------|------|------|------|------|------|
| Kushimoto, Kinki, Japan                        | 7940   | 0.9 | 7.5 | 10.5 | 12.2 | 7.4  | 8.8  | 9.2  | 9.6  | 10.0 | 10.5 | 11.0 |
| Tosashimizu, Shikoku, Japan                    | 8080   | 0.9 | 7.6 | NC   | 11.2 | 7.5  | 9.0  | 9.4  | 9.8  | 10.2 | 10.7 | 11.2 |
| Amamioshima Kominato, Kyushu, Japan            | 8040   | 1.2 | 7.6 | 10.5 | 10.7 | 7.4  | 8.9  | 9.3  | 9.7  | 10.2 | 10.6 | 11.2 |
| Clearwater beach, the USA (Caribbean Sea)      | 11,310 | 0.3 | NC  | NC   | 30.7 | 10.5 | 12.6 | 13.1 | 13.7 | 14.3 | 15.0 | 15.7 |
| Crotone, Italy (Mediterranean Sea)             | 17,650 | 0.3 | 17  | NC   | 23   | 16.3 | 19.6 | 20.4 | 21.3 | 22.3 | 23.3 | 24.5 |
| Ponta Delgada, Portugal (North Atlantic Ocean) | 16,550 | 0.7 | NC  | 24   | 27.5 | 15.3 | 18.4 | 19.2 | 20.0 | 20.9 | 21.9 | 23.0 |
| Takoradi, Ghana (South Atlantic Ocean)         | 18,160 | 0.5 | 17  | NC   | 21   | 16.8 | 20.2 | 21.0 | 21.9 | 22.9 | 24.0 | 25.2 |
| Pt. Louis, Mauritius (West Indian Ocean)       | 12,710 | 0.3 | 12  | NC   | 24.3 | 11.8 | 14.1 | 14.7 | 15.3 | 16.0 | 16.8 | 17.7 |

276

277 (2) West coasts of the United States

278 Conversely, a 1 m class tsunamis were observed at the coasts of California, which were more than 8000  
 279 km away from the volcano. Figure 3b indicates that the atmospheric pressure waves with a traveling velocity  
 280 in the range of 210–220 m/s predominantly generate tsunamis with a maximum possible, amplitude of  
 281 approximately 0.1 m off these coasts. Figure 3c indicates that the maximum possible amplitudes depicted in  
 282 Fig. 3b are achievable; thus, tsunamis with an amplitude of 0.5 m could reach the coasts. In contrast, when the  
 283 traveling velocity of atmospheric pressure wave is 200 m/s, Fig. 3c indicates that tsunamis are not sufficiently  
 284 amplified near offshore of the Western America. In North America, the largest tide level displacement of 1.3  
 285 m was recorded in San Luis, California, and the next largest tide level displacement of 1.1 m was observed at  
 286 the port of Crescent City, 8470 km and 8710 km away from the eruption site, respectively. At these locations,  
 287 the largest tide level fluctuations started approximately 12 h after the eruption, which was in harmony with the  
 288 estimated arrival times of the tsunamis due to the atmospheric pressure waves with a traveling velocity in the  
 289 range of 210–220 m/s.

290 (3) West coasts of South America

291 Tsunamis with a height of over 1 m were observed in a wide area of Chilian coasts, which were about  
 292 10,000 km away from the eruption site. Especially at the coast of Coquimbo, the largest class tide level  
 293 fluctuations of 1.9 m were observed. As the phase velocity of shallow water waves is approximately 200–210  
 294 m/s offshore Coquimbo, the Proudman resonance efficiently occurred owing to the atmospheric pressure waves  
 295 with a traveling velocity in the range of 200–210 m/s. Moreover, there were ridges parallel to the path of the  
 296 atmospheric pressure waves offshore, which could amplify the tsunami amplitude beyond the maximum  
 297 possible amplitude. The maximum tide level fluctuations started to be amplified 14–15 h after the eruption and  
 298 showed the maximum value around 17.5 h after the eruption. The distance between Coquimbo and the eruption  
 299 site is 10,160 km, indicating that the arrival time of the tsunamis in the above mode matched the amplification  
 300 start time of the maximum waves.

301 (4) Other sea areas beyond lands

Furthermore, tsunamis were also observed along the Mediterranean coasts. For example, in Crotone, Italy, the tide level fluctuations started about 17 h after the eruption, and the maximum amplitude of approximately 0.3 m was recorded 23 h later than the eruption time<sup>13</sup>. Based on the data shown in Fig. 3b, tsunamis due to the atmospheric Lamb wave with a traveling velocity of 300–310 m/s can be predominant in the Mediterranean. According to the analysis of atmospheric Lamb waves<sup>14</sup>, over the Mediterranean, an atmospheric Lamb wave traveled from northeast to southwest approximately 16.5 h after the eruption, and another atmospheric Lamb wave propagated in the opposite direction from southwest to northeast approximately 20 h after the eruption. The maximum tide level fluctuations appeared nearly 23 h after the eruption; thus, the tsunamis due to these two atmospheric Lamb waves could be trapped and resonated in the Mediterranean.

Although tsunamis of several tens of centimeters were observed in the Caribbean Sea, Indian Ocean, and Atlantic Ocean, a clear relationship was not found between the excitation source and the start time of the maximum tide level fluctuations based on Tab. 2, which provides the estimated arrival times of tsunamis considering atmospheric pressure waves in one direction. In these areas, which are located far from the eruption site, atmospheric pressure waves arriving from opposite directions could have a significant effect as in the Mediterranean, requiring further analysis. However, as at the Pacific coasts, the initial time of the tide level fluctuations started slightly later than the arrival time of the atmospheric Lamb waves at the coasts of the Mediterranean Sea, the Caribbean Sea, the Indian Ocean, and the Atlantic Ocean.

At several locations in the world, the tide level slightly dropped<sup>13</sup> when the atmospheric Lamb waves arrived. The drop in the tide level could occur because of forced waves following an atmospheric Lamb wave.

The offshore waters of each coast in the world selectively respond to atmospheric pressure wave components with traveling velocities from 200 m/s to 300 m/s, depending on the water depth, and excite significant tsunamis. Large tsunamis were observed at the coasts with such an excitation water on the path of the atmospheric pressure waves, and the estimated time when the tsunamis generated at these excitation waters reached the coasts was in good agreement with the time when the large tsunamis appeared at the coasts. Thus, the global tsunami height distribution was created by the tsunamis excited in waters with various water depths at different times.

### 328 (5) Japanese coasts

Using the seawater depth depicted in Fig. 4a, the distributions of the maximum possible amplitude  $H_{\max}$  based on Eq. (M8) and the resonance distance  $\lambda_{\max}$  based on Eq. (M7) are presented in Fig. 4b for various traveling velocities of atmospheric pressure waves. Moreover, Fig. 4c shows the distributions of the maximum possible amplitude converted to the values at a water depth of 5 m by the Green law from  $H_{\max}$  presented in Fig. 4b.

Off the coasts of Japan, the phase velocities of predominant tsunamis are 240 m/s off eastern Japan, 200 to 210 m/s off both Shikoku and Kinki, 220 m/s off the northern Nansei Islands, 240 m/s off the southern Nansei Islands, and 230 to 240 m/s off Ogasawara Islands near the Mariana Trench and Ridge. The difference between the arrival time of the atmospheric pressure waves and the estimated arrival time of the predominant tsunamis described in Tab. 2 was 20–40 min at Chichijima, approximately 50 min at Kuji Port, and 20–30 min

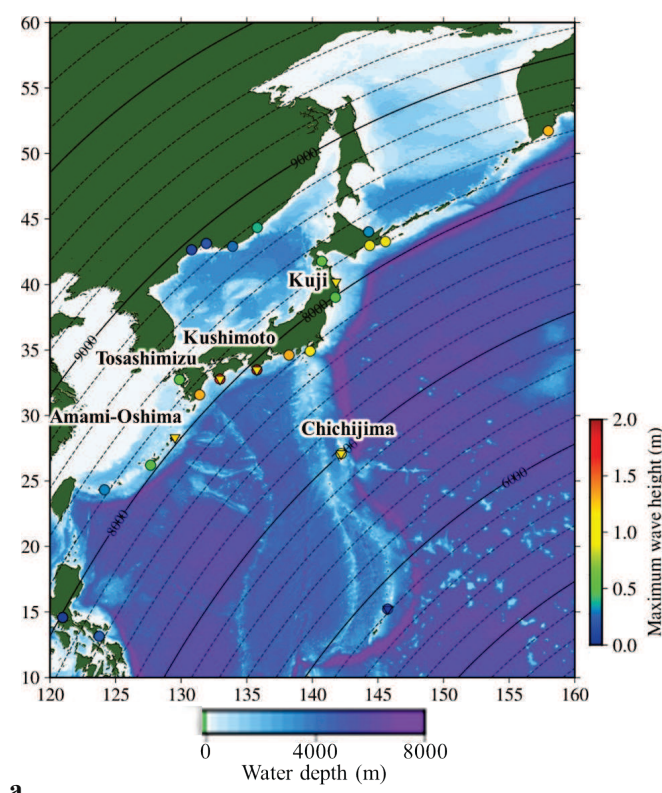
339 at other locations. The tsunami arrival time  $t_{\text{tsunami}}$  was in harmony with the start time of the tide level  
340 fluctuations and the appearance time of the maximum tide level fluctuations.

341 Especially at Amami, 8040 km away from the eruption site, the observed maximum tide level  
342 displacement was 1.2 m, around 10 h 30 min after the eruption. The predominant traveling velocity of tsunamis  
343 is 230 m/s off Amami, and the distance between Amami and the shelf is about 50 km. Assuming that the average  
344 water depth on the shelf is 100 m, the arrival time of the tsunamis at Amami is 10 h 37 min after the eruption.  
345 Therefore, these tsunamis appeared as the largest tide level fluctuations at Amami. Between Tonga and Amami,  
346 there are three or four ridge-shaped sudden changes in water depth, such as the Mariana Ridge; thus, the  
347 tsunami amplitude off Amami could be amplified up 3 to 4 times based on the above-described mechanism.

348 Moreover, on the way to Amami from the eruption site, there were sudden changes in water depth  
349 including the Mariana Ridge, so the tsunami height excited by atmospheric pressure waves could be amplified  
350 over the changes in water depth<sup>12</sup>.

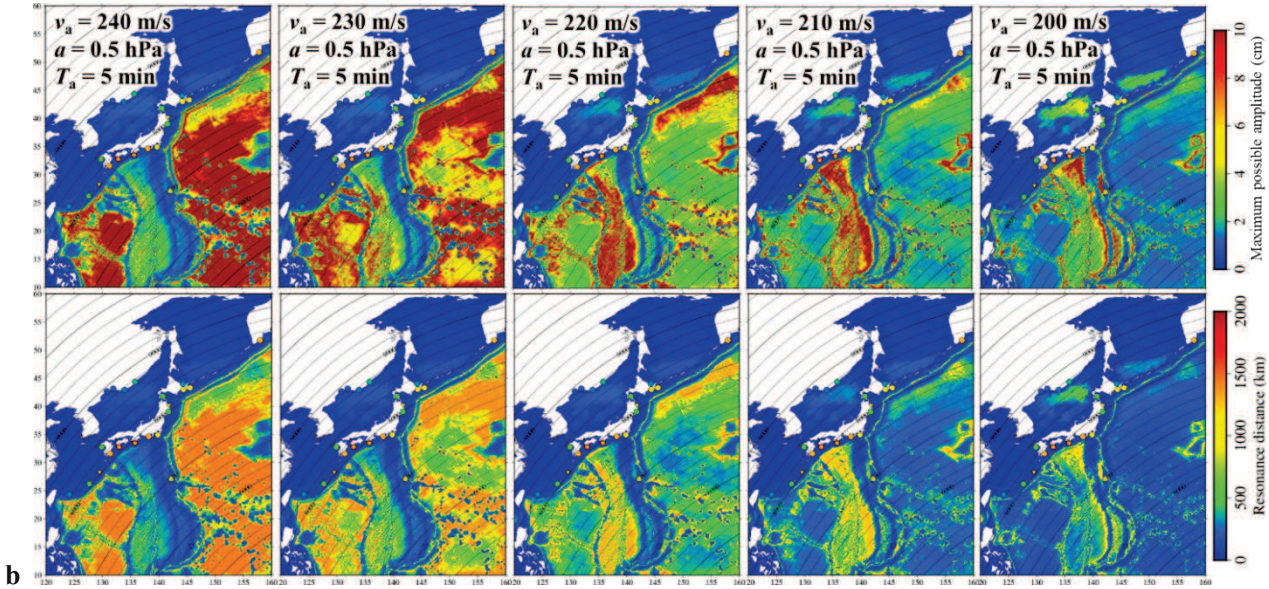
351

352 **Fig. 4: Estimation of tsunamis excited by atmospheric pressure wave around Japan.**



353

354



355

356 **a** Maximum tsunami heights at various locations around Japan, due to the 2022 Tonga eruption. The data  
 357 indicated by  $\circ$  and  $\nabla$  are the maximum total amplitudes<sup>2</sup> and the maximum tsunami heights from the  
 358 observed data<sup>13</sup>, respectively. The color map presents the bathymetry of GEBCO. The isolines indicate the  
 359 distance from the eruption site every 200 km. **b** Distributions of the maximum possible amplitude  $H_{\max}$   
 360 obtained from Eq. (M8) (upper) and the resonance distance  $\lambda_{\max}$  obtained from Eq. (M7) (lower) for various  
 361 traveling velocities of atmospheric pressure waves. The isolines indicate the distance from the site of the 2022  
 362 Tonga eruption every 200 km. The maximum absolute value of the atmospheric pressure,  $a$ , and the period of  
 363 the pulse,  $T_a$ , were 0.5 hPa and 5 min, respectively. The seawater density  $\rho$  was assumed to be  $1020 \text{ kg/m}^3$ . The  
 364 maximum possible amplitude  $H_{\max}$  and resonance distance  $\lambda_{\max}$  were calculated, assuming that the upper limit  
 365 of the maximum possible amplitude was 0.1 m. **c** Distributions of the maximum possible amplitude converted  
 366 to the values at a water depth of 5 m by the Green law from  $H_{\max}$  evaluated by Eq. (M8) for various traveling  
 367 velocities of atmospheric pressure waves. The maximum absolute value of the atmospheric pressure,  $a$ , and  
 368 the period of the pulse,  $T_a$ , were 0.5 hPa and 5 min, respectively. The seawater density  $\rho$  was assumed to be  
 369  $1020 \text{ kg/m}^3$ .

370

371 **Tsunamis caused by atmospheric pressure waves due to several historical large eruptions**

372 Why did the atmospheric pressure waves due to the previous large eruptions not cause significant tsunamis  
 373 like the case of the 2022 Tonga eruption? To answer this question, we summarized the atmospheric pressure  
 374 and the maximum tide level displacement observed at each location in Japan, due to several historical volcanic  
 375 eruptions in Tab. 3a along with the data of the 2022 Tonga eruption. The historical eruptions are the 1883  
 376 Krakatau, 1956 Bezymianny, 1958 Asama, 1980 St. Helens, and 1991 Pinatubo volcanic eruptions, the data of  
 377 which were obtained from the references indicated in Tab. 3b.

378

379 **Tab. 3 Historical volcanic eruption properties observed in Japan.** **a** Atmospheric pressure and tide level  
 380 displacement observed at each location in Japan due to several volcanic eruptions. The data were obtained  
 381 from the references indicated in Tab. 3b. The traveling velocity  $v_a$  in the table is that of the first atmospheric  
 382 pressure wave that reached the location. **b** Sources of the data listed in Tab. 3a. The numbers 1 to 6 in Tab. 3b  
 383 are the same as those in Tab. 3a.

| No. | Eruption Day (JST) | Volcano                           | Location                | Eruption Type             | Estimated VEI | Atmospheric pressure Waves          |                    |                                | Maximum Tide Level Displacement at Each Location (m)  |
|-----|--------------------|-----------------------------------|-------------------------|---------------------------|---------------|-------------------------------------|--------------------|--------------------------------|---|
|     |                    |                                   |                         |                           |               | Maximum Displacement $\alpha$ (hPa) | Period $T_a$ (min) | Traveling Velocity $v_a$ (m/s) |   |
| 1   | Aug. 27, 1883      | Krakatau, Indonesia               | 6.1024 S<br>105.4229 E  | Land, partially submarine | 6             | < 0.5                               | 30                 | 271                            | 0.1 m at Kuwana   |
| 2   | Mar. 30, 1956      | Bezymianny, Kamchatka             | 55.9779 N<br>160.5870 E | Land                      | 5             | 0.5–1.0                             | 12–13              | 310–317                        | -   |
| 3   | Nov. 10, 1958      | Asama, Japan                      | 36.4064 N<br>138.5231 E | Land                      | 1             | 0.1–0.3                             | 0.2–1              | 280                            | -   |
| 4   | May 18, 1980       | St. Helens, West Coast of the USA | 45.8244 N<br>122.1940 W | Land                      | 5             | 0.1–0.2                             | 3–5                | 308                            | -   |
| 5   | Jun. 15, 1991      | Pinatubo, Philippines             | 15.1446 N<br>120.3499 E | Land                      | 6             | 0.0173                              | 0.25               | 280                            | -   |
| 6   | Jan. 15, 2022      | Hunga Tonga-Hunga Ha'apai, Tonga  | 20.5418 S<br>175.3940 W | Submarine                 | 6             | 2.0                                 | 20–30              | 300–310                        | 0.9 m at Chichijima<br>0.9 m at Kushimoto<br>0.9 m at Tosashimizu<br>1.2 m at Amami<br>1.1 m at Kuji Port |

384

| No. | Data Sources   |
|-----|--|
| 1   | Burt <sup>15</sup> , Kobayashi and Kakinuma <sup>16</sup> , Murayama <sup>17</sup>           |
| 2   | Kobayashi and Kakinuma <sup>16</sup> , Murayama <sup>17</sup>                                |
| 3   | Koike <sup>18</sup> , Tanaka <sup>19</sup>   |
| 4   | Tanaka <sup>19</sup>   |
| 5   | Tahira <sup>20</sup>   |
| 6   | Study session on tsunami prediction technology <sup>1</sup> , Nakajo, S. et al., Weathernews |

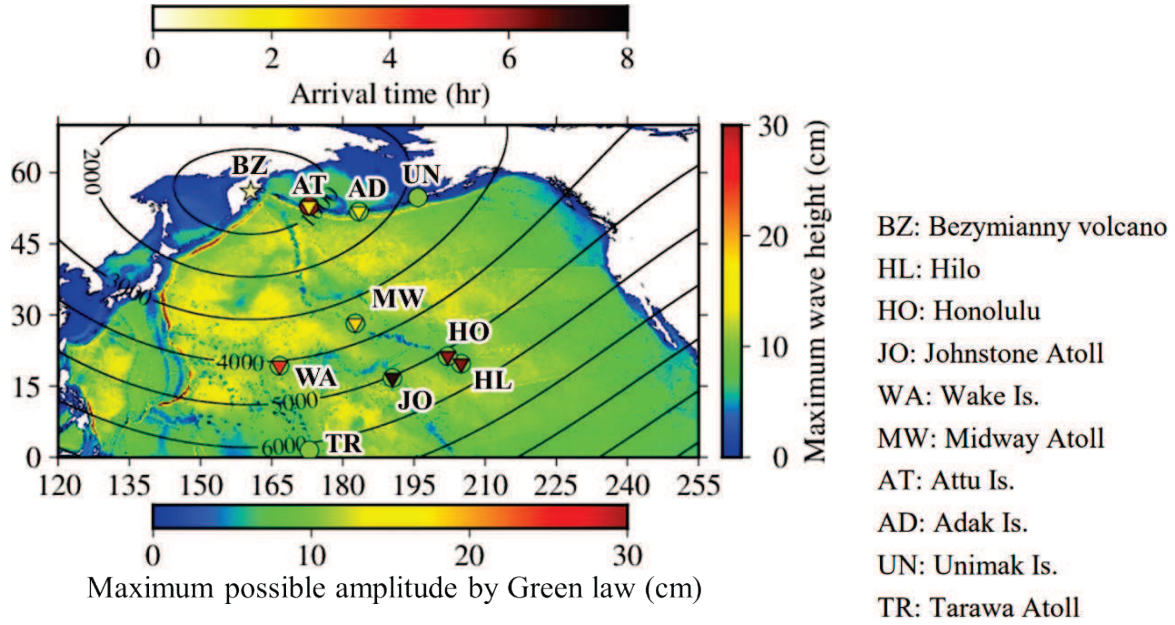
385

386 Based on Tab. 3a, there are three characteristics of the 2022 Tonga eruption as follows:

- 387 (1) The eruption was a submarine volcanic eruption.  
 388 (2) The maximum displacement of atmospheric pressure waves was larger than that of the previous eruptions.  
 389 (3) The representative period of atmospheric pressure waves was longer than that of the previous eruptions.

390 The pressure deviation and wave period of the atmospheric pressure waves due to the 2022 Tonga eruption  
 391 were the largest. Among the eruptions described in Tab. 3a, only the 2022 Tonga eruption caused atmospheric  
 392 pressure waves that generated tsunamis with an amplitude over 1 m. For example, in the case of the 1958  
 393 Bezymianny volcanic eruption, the pressure deviation of the atmospheric pressure waves was 0.5–1.0 hPa.  
 394 Figure 5 depicts the distribution of the maximum possible amplitude converted to the value at a water depth  
 395 of 5 m by the Green law from  $H_{\max}$  evaluated by Eq. (M8) in which  $v_a = 310 \text{ m/s}$ ,  $a = 1.0 \text{ hPa}$ , and  $T_a = 13 \text{ min}$ .  
 396 The estimated maximum possible amplitude, which can explain the observed maximum tide level  
 397 displacements in the North Pacific<sup>16,21</sup>, was smaller than that due to the 2022 Tonga eruption.

398  
 399 **Fig. 5: Estimation of tsunamis excited by the 1956 Bezymianny eruption.**



400 Distribution of maximum possible amplitude converted to the value at a water depth of 5 m by the Green law  
 401 from  $H_{\max}$  evaluated by Eq. (M8) in which  $v_a = 310 \text{ m/s}$ ,  $a = 1.0 \text{ hPa}$ , and  $T_a = 13 \text{ min}$ . The observed tsunami  
 402 height and arrival time of the tsunamis caused by the atmospheric pressure waves due to the 1956 Bezymianny  
 403 eruption<sup>16</sup> are denoted by  $\circ$  and  $\nabla$ , respectively. The mark  $\star$  indicates the site of the eruption, the distance  
 404 from which is indicated by the isolines every 1000 km.

406 One of the reasons for the large pressure deviation is that the eruption occurred in the sea. Some of the  
 407 most powerful eruptions occurred through water<sup>22</sup>. In subsea volcanic eruptions, seawater rapidly expands  
 408 because of the reaction with magma, whereas the decompression effect of hydrostatic pressure increases in  
 409 proportion to the water depth at the crater, suppressing ejecta above the sea surface<sup>23,24</sup>. Thus, a submarine

eruption is significantly different from a land eruption based on not only the internal mechanism of the eruption itself but also the external mechanism of the balance between the water pressure and the reaction of seawater and magma. Due to the eruption that occurred on January 14, the crater was submerged below the sea surface, resulting in a crater depth of approximately 200 m<sup>22</sup>. The water depth at the crater was as thin as a water film compared with the crater depth of several thousands of meters, which is common for a submarine volcano. This water film could not suppress the thermal expansion and gas generation of seawater; instead, it made the eruption shocking. Such a shocking eruption could effectively shake the air above<sup>25</sup>.

Moreover, the period of the atmospheric pressure waves due to the previous eruptions was shorter than that of the 2022 Tonga eruption. If these atmospheric pressure waves were atmospheric Lamb waves, the subsequent atmospheric waves were even shorter, depending on the eruption scale. Therefore, the dispersion effect was stronger in the generation and propagation processes of the tsunamis due to the previous eruptions than in the case of the 2022 Tonga eruption, resulting in the observed smaller tsunami amplitude. If an eruption produces an atmospheric pressure wave the pressure deviation and wavelength are larger than those in the 2022 Tonga eruption larger tsunamis can be generated.

Atmospheric pressure waves can generate tsunamis in water areas regardless of the distance from the eruption site, including water areas after crossing islands and continents. Therefore, a global network of atmospheric pressure information is required to quickly determine the response policy against both eruption tsunamis and meteotsunamis due to atmospheric pressure waves.

## Methods

### ***Formulas for the estimation of the maximum possible amplitude and resonance distance of tsunamis due to atmospheric pressure waves***

We considered one-dimensional propagation problems of tsunamis generated by atmospheric pressure waves. We assumed that an atmospheric pressure wave is a pulsed wave traveling with a constant velocity of  $v_a$  and that it travels in the positive direction of the  $x$ -axis over a water area with a uniform still water depth of  $h$ . An estimation equation for the maximum possible amplitude of a tsunami under the influence of an atmospheric pressure wave, namely  $H_{P,\max}$ , was derived as follows<sup>8</sup>:

$$H_{P,\max} = \frac{a}{\rho g} \left| 1 - \left( \frac{v_a}{\sqrt{gh}} \right)^2 \right|^{-1}, \quad (\text{M1})$$

where  $a$  (Pa) is the maximum absolute value of the atmospheric pressure  $p$ ,  $\rho$  is the water density, and  $g$  is the gravitational acceleration, namely 9.8 m/s<sup>2</sup>. Equation (M1) represents the maximum amplitude of the composite wave consisting of a forced wave balanced by the atmospheric pressure and a resonant wave excited by the progress of the atmospheric pressure wave. This composite wave propagates below the pressure wave in water with a uniform still water depth, but when it crosses a sudden change in water depth, for example,

444 from deep water to shallow water, the latter resonant wave separates from the pressure wave.

445 In the present study, focusing on the latter resonance wave, we introduce the important parameters related  
 446 to the resonance limit, and consider the maximum possible amplitude of tsunamis that have been generated by  
 447 an atmospheric pressure wave and left the influence of the atmospheric pressure wave. When an atmospheric  
 448 pressure wave profile is an isosceles triangle, the atmospheric pressure deviation at location  $x$  during time  $\Delta t$ ,  
 449 namely  $\Delta p(x, t)$ , is

$$450 \quad \Delta p(x, t) = \begin{cases} \frac{a}{0.5L_a} v_a \Delta t & \text{when } x_0 + v_a \Delta t \leq x \leq x_0 + 0.5L_a + v_a \Delta t \\ -\frac{a}{0.5L_a} v_a \Delta t & \text{when } x_0 - 0.5L_a + v_a \Delta t \leq x < x_0 + v_a \Delta t \end{cases}, \quad (\text{M2})$$

451 where  $L_a$  is the wavelength of the pulse.  $L_a$  is  $v_a T_a$ , where  $T_a$  (s) denotes the period of the pulse. The location at  
 452 which the pulse shows the maximum or minimum value is  $x_0$  at the initial time  $t_0$ .

453 From  $t_0$  to  $t_0 + \Delta t$ , an atmospheric pressure pulse travels at a distance of  $v_a \Delta t$ , as illustrated in Fig. 6. When  
 454  $a > 0$ , the pulse pushes down the water surface under its front half and lifts the water surface under its back  
 455 half. To balance these forces, a free positive wave is generated under its front half, whereas a free negative  
 456 wave is generated under its back half. In this process, the following potential energy  $\Delta\eta$ , balancing with  
 457 pressure deviation  $\Delta p$ , is given to the water to generate free water waves during the time  $\Delta t$ :

$$458 \quad \Delta\eta(x, t) = \frac{\Delta p}{\rho g} = \begin{cases} \frac{a}{0.5L_a \rho g} v_a \Delta t & \text{when } x_0 + v_a \Delta t \leq x \leq x_0 + 0.5L_a + v_a \Delta t \\ -\frac{a}{0.5L_a \rho g} v_a \Delta t & \text{when } x_0 - 0.5L_a + v_a \Delta t \leq x < x_0 + v_a \Delta t \end{cases}. \quad (\text{M3})$$

459 In the derivation of Eq. (M3), water waves are assumed to be linear shallow water waves. The potential  
 460 energy given by Eq. (M3) is separated in the positive and negative directions of the  $x$ -axis, resulting in two  
 461 free waves with an amplitude of  $0.5\Delta\eta$  and phase velocities of  $\sqrt{gh}$  and  $-\sqrt{gh}$ , respectively, where an  
 462 amplitude is defined by the vertical displacement from the still water surface to the highest or lowest water  
 463 surface of a water wave, with a positive or negative value, respectively.

464 Focusing on the water wave propagating in the positive direction of the  $x$ -axis, which is the same as the  
 465 traveling direction of the atmospheric pressure wave, the amplitude  $H(t)$  and wavelength  $L(t)$  of the resonant  
 466 water wave, namely tsunami, due to the atmospheric pressure wave are evaluated by the linear superposition  
 467 of the waves generated at each time step  $\Delta t$ , resulting in the integration with regard to  $t$  as follows:

$$468 \quad H(t) = \frac{a}{L_a \rho g} v_a t = \frac{a}{T_a \rho g} t, \quad (\text{M4})$$

$$469 \quad L(t) = \frac{1}{2} L_a + |v_a - \sqrt{gh}| t. \quad (\text{M5})$$

470 As indicated by Eq. (M4), the tsunami amplitude is proportional to time  $t$ . The tsunami grows only when

it overlaps with the atmospheric pressure wave; thus, the maximum tsunami amplitude depends on the resonance time  $\tau_{\max}$  during which they overlap. The resonance time  $\tau_{\max}$ , and the distance they travel while overlapping, namely resonance distance  $\lambda_{\max}$ , are described by

$$\tau_{\max} = \frac{L_a}{2|v_a - \sqrt{gh}|} = \frac{v_a T_a}{2|v_a - \sqrt{gh}|}, \quad (\text{M6})$$

$$\lambda_{\max} = v_a \tau_{\max}. \quad (\text{M7})$$

Based on Eqs. (M4), (M5), and (M6), the maximum possible amplitude  $H_{\max}$  and the maximum possible wavelength  $L_{\max}$  are described by

$$H_{\max} = H(\tau_{\max}) = \alpha \tau_{\max} = \frac{a}{\rho g} \left( 2 \left| 1 - \frac{\sqrt{gh}}{v_a} \right| \right)^{-1}, \quad (\text{M8})$$

$$L_{\max} = L(\tau_{\max}) = L_a, \quad (\text{M9})$$

where  $\alpha$  (m/s) is the tsunami amplitude amplification factor.

After the resonance time  $\tau_{\max}$ , resonant waves are continuously generated and extinguished under both the front and back halves of the atmospheric pressure wave, as described below. As an example, we consider the water surface response when  $v_a > \sqrt{gh}$  and  $a > 0$ . From  $t_0$ , at which the atmospheric pressure wave starts to travel, to  $t_0 + \tau_{\max}$ , tsunamis with amplitudes of  $H_{\max}$  and  $-H_{\max}$ , namely tsunamis  $A_0$  and  $B_0$ , respectively, are generated under the front and back halves of the atmospheric pressure wave, respectively. Thereafter, from  $t_0 + \tau_{\max}$  to  $t_0 + 2\tau_{\max}$ , tsunamis  $A_1$  and  $B_1$  are similarly generated under the front and back halves of the atmospheric pressure wave, respectively. Thus, from  $t_0 + i \cdot \tau_{\max}$  to  $t_0 + (i+1) \cdot \tau_{\max}$ , tsunamis  $A_i$  and  $B_i$ , with positive and negative amplitudes, respectively, are generated for  $i = 1, 2, \dots, I$ . After  $t_0 + \tau_{\max}$ , tsunami  $A_{i-1}$  with a positive amplitude is canceled by tsunami  $B_i$  with a negative amplitude that is newly generated under the back half of the atmospheric pressure wave. At the same time, tsunami  $A_i$  with a positive amplitude is generated under the front half of the atmospheric pressure wave.  $A_i$  is generated and  $A_{i-1}$  is extinguished under the front half of the atmospheric pressure wave; thus,  $A_i$  propagates at a phase velocity of  $v_a$  like a forced water wave following the atmospheric pressure wave. Notably, the apparent wave height of  $A_i$  is smaller than  $H(t)$  and  $H_{\max}$ , because a forced water wave with a negative amplitude is superimposed on  $A_i$ . Conversely,  $B_0$  with a negative amplitude, which was generated under the back half of the atmospheric pressure wave from  $t_0$  to  $t_0 + \tau_{\max}$ , is not affected by  $A_i$  and  $B_i$ ; thus, it propagates at a phase velocity of  $\sqrt{gh}$  without disappearing. The tsunamis generated by atmospheric pressure waves separate from the atmospheric pressure waves, for example, because of a sudden change in water depth, and the transmission and reflection in that case were explained by a linear theory<sup>11</sup>.

Therefore, two types of tsunamis, namely  $A_i$  and  $B_0$ , with amplitudes of  $H_{\max}$  and  $-H_{\max}$ , respectively, propagate at different phase velocities  $v_a$  and  $\sqrt{gh}$ , respectively. The period of  $A_i$  coincides with that of the atmospheric pressure wave,  $T_a$ , under the influence of the atmospheric pressure wave; however, after  $A_i$  leaves

503 the influence of the atmospheric pressure wave, the period of  $A_i$  is equal to that of  $B_0$ :

504

$$T_{\max} = \frac{L_{\max}}{\sqrt{gh}} = \frac{v_a}{\sqrt{gh}} T_a . \quad (\text{M10})$$

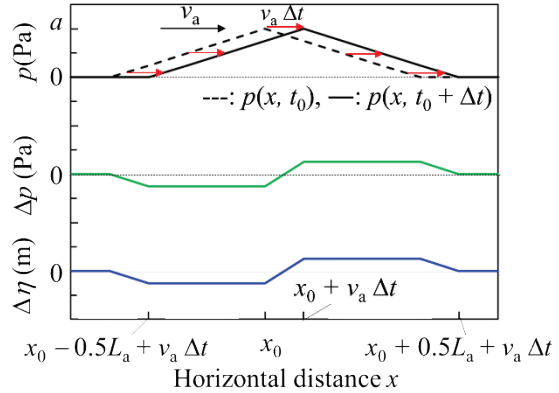
505 The maximum possible amplitude  $H_{\max}$  evaluated by Eq. (M8) represents the amplitude of a tsunami that  
506 has left the influence of an atmospheric pressure wave.

507 Moreover, in two-dimensional propagation problems not covered here, the wave amplitude of  $A_i$  is  
508 attenuated by the directional dispersion only within the resonance time, because  $A_i$  exists only during the  
509 resonance time, whereas the amplitude attenuation of  $B_0$  continues after  $t = t_0$ , leading to differences in not  
510 only phase velocity but also amplitude characteristics between  $A_i$  and  $B_0$ . In this study, the multidirectional  
511 effects of tsunamis are not considered; thus, two-dimensional analyses with more complicated bathymetries  
512 are required in the future.

513

514 **Fig. 6: Sketch of a traveling atmospheric pressure wave and resultant displacements of pressure and**

515 water surface during time  $\Delta t$ .



516

517 The broken and solid black lines indicate the atmospheric pressure wave profiles at  $t = t_0$  and  $t = t_0 + \Delta t$ ,  
518 respectively. The green and blue lines indicate pressure deviation and potential energy, respectively.

## 520 Numerical method

521 The above-described formula for the maximum possible amplitude of tsunamis was verified numerically  
522 by simulating the one-dimensional propagation of tsunamis due to an atmospheric pressure wave using two  
523 numerical models, namely nondispersion and weak dispersion models. The governing equations of the former  
524 are described by the following nonlinear shallow water equations:

525

$$\frac{\partial(\eta + h)}{\partial t} + \frac{\partial Q}{\partial x} = 0 , \quad (\text{M11})$$

526

$$\frac{\partial Q}{\partial t} + \frac{\partial}{\partial x} \left( \frac{Q^2}{\eta + h} \right) = -g(\eta + h) \frac{\partial \eta}{\partial x} - \frac{1}{\rho} \frac{\partial p}{\partial x} , \quad (\text{M12})$$

527 where  $\eta(x, t)$ ,  $Q(x, t)$ ,  $h(x, t)$ , and  $p(x, t)$  are the water surface displacement, horizontal flow rate in the  $x$ -axis  
 528 direction, still water depth, and pressure on the water surface.

529 Further, the governing equations of the latter are given by the following Boussinesq-type equations:

$$530 \quad \frac{\partial(\eta + h)}{\partial t} + \frac{\partial Q}{\partial x} = 0, \quad (\text{M13})$$

$$531 \quad \frac{\partial Q}{\partial t} + \frac{\partial}{\partial x} \left( \frac{Q^2}{\eta + h} \right) = -g(\eta + h) \frac{\partial \eta}{\partial x} - \frac{1}{\rho} \frac{\partial p}{\partial x} + \frac{h^2}{3} \frac{\partial^3 Q}{\partial t \partial x^2}, \quad (\text{M14})$$

532 which were proposed and used<sup>26</sup> by referring to the dispersion term<sup>27</sup>, and also applied to calculate the  
 533 dispersive tsunamis<sup>28</sup>.

534 Equations (M11)–(M14) were modified to finite-difference equations and solved numerically, where the  
 535 grid size  $\Delta x$  was 250 m, and the time interval  $\Delta t$  was 0.05 s. The Sommerfeld radiation condition was assumed  
 536 at the lateral boundaries.

### 538 Components of atmospheric pressure waves due to the 2022 Tonga eruption

539 The atmospheric pressure waves due to the 2022 Tonga eruption included the wave components of  
 540 different traveling velocities, as indicated in Figs. 7a and 7b, obtained in Amami and Arita, Japan, respectively.  
 541 We assumed that the occurrence time of the 2022 Tonga eruption,  $t_e$ , was 13:15 on January 15, 2022 (JST).  
 542 Figure 7c depicts the wavelet analysis for the data presented in Fig. 7b.

543 Assuming that all atmospheric pressure waves occurred at the eruption site and traveled concentrically,  
 544 the following atmospheric pressure wave components were extracted from the data of Amami and Arita,  
 545 Japan<sup>1</sup>:

546 (1) A pulse-like atmospheric pressure fluctuation with a traveling velocity in the range of 300–310 m/s, namely  
 547 atmospheric Lamb wave<sup>5,14</sup>. The maximum displacement was approximately 2 hPa, and the wave period  
 548 was 25–30 min. The fluctuations started approximately 7 h and 15 min after the eruption.

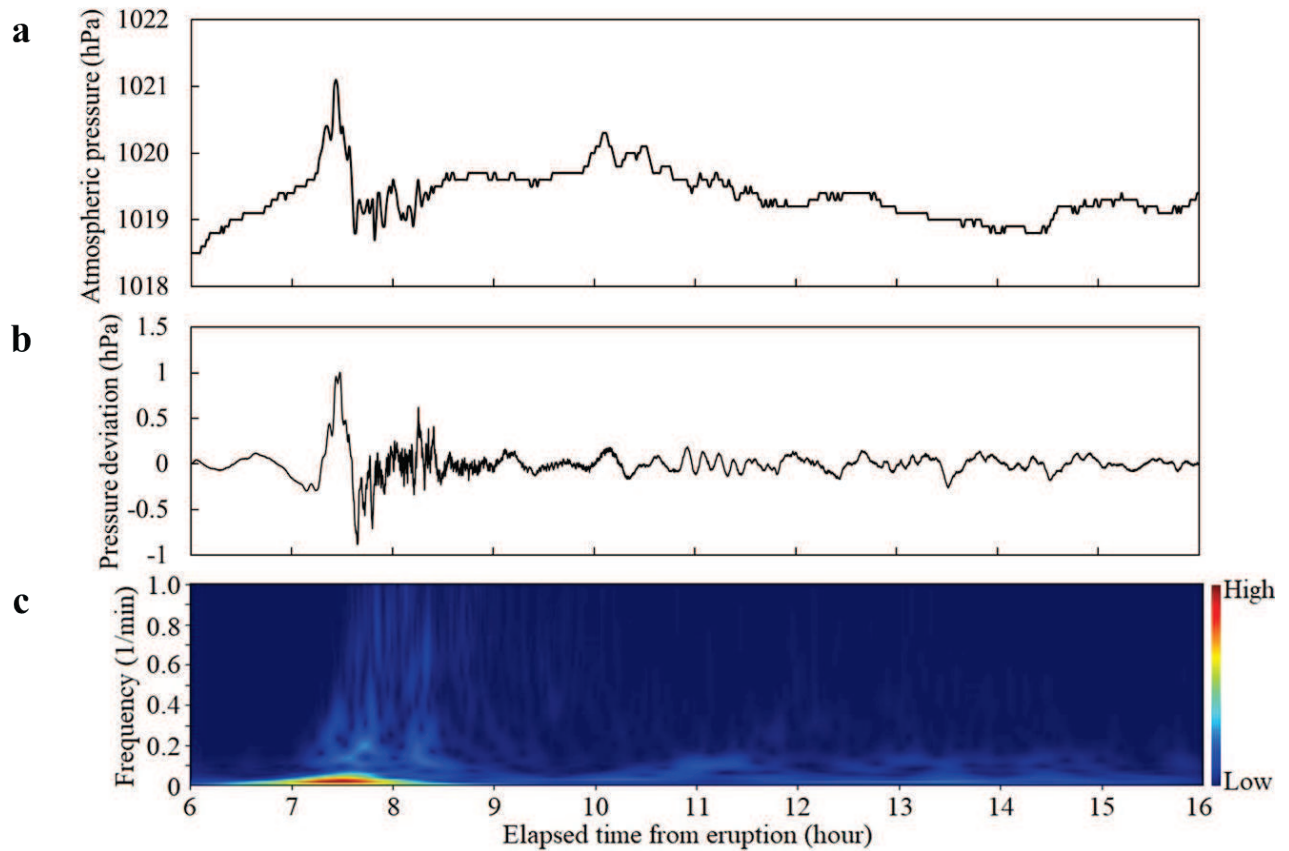
549 (2) Atmospheric pressure fluctuations with a traveling velocity in the range of 230–300 m/s. The maximum  
 550 displacement was 0.1–0.5 hPa and the period was 5 min or less. The fluctuations started 7 h and 15 min  
 551 after the eruption. The fluctuations lasted for approximately 2 h.

552 (3) Atmospheric pressure fluctuations with a traveling velocity in the range of 210–250 m/s. The maximum  
 553 displacement was approximately 0.3 hPa, and the wave period was 30–60 min.

554 (4) Atmospheric pressure fluctuations with a traveling velocity of 210 m/s or less. The maximum displacement  
 555 was approximately 0.3 hPa, and the wave period was in the range of 5–10 min. The fluctuations lasted for  
 556 approximately 1 h.

557 The traveling velocities of the subsequent atmospheric pressure waves, including sound and atmospheric  
 558 gravity waves, were slower if they were gradually generated by the progress of the atmospheric Lamb wave.

560 **Fig. 7: Atmospheric pressures observed in Amami and Arita, Japan, from 19:15 on January 15 to 5:15**  
 561 **on January 16, 2022.**



562  
 563 **a** Time variation of the atmospheric pressure in Amami, Kagoshima, Japan, observed every one minute by  
 564 Weathernews meteorological observer “Soratena.” **b** Atmospheric pressure deviation in Arita, Wakayama,  
 565 Japan. The data obtained by Nakajo, S. et al. with a sampling frequency of 100 Hz was downsampled to 1 Hz  
 566 and processed by a high-pass filter with a passing frequency of 1/3600 Hz and a blocking frequency of 1/(5 ×  
 567 3600) Hz. **c** Wavelet analysis result of the atmospheric pressure deviation depicted in Fig. 7b.

#### 569 *Estimations of arrival time*

570 The tsunami propagation direction is assumed to be along the straight line connecting the eruption site  
 571 and the tsunami observation locations. Based on Fig. 3b, we first extracted the traveling velocities of  
 572 atmospheric pressure waves that could excite tsunamis with large  $H_{\max}$  in a relatively wide excitation area.  
 573 Subsequently, based on Fig. 3c, when the distance between the excitation area and tsunami observation location  
 574 is longer than the resonance distance  $\lambda_{\max}$ , we evaluated whether the maximum possible amplitude  $H_{\max}$  was  
 575 achieved. The maximum tsunami amplitude depends on both the length of the excitation area and the resonance  
 576 distance on the path of atmospheric pressure waves.

577 We also obtained the estimated arrival time  $t_{\text{tsunami}}$ , at which the tsunamis reached the tsunami observation  
 578 locations. The time  $t_{\text{tsunami}}$  was the sum of time  $t_{\text{edge}}$ , at which the corresponding atmospheric pressure wave  
 579 reached the edge of the excitation area closest to the tsunami observation location, and time  $\Delta t_{\text{coast}}$ , that is, the

580 time for tsunami propagation from the edge to the tsunami observation location. Therefore, the estimated  
581 arrival time  $t_{\text{tsunami}}$  was evaluated by

$$\left. \begin{aligned} t_{\text{tsunami}} &= t_{\text{edge}} + \Delta t_{\text{coast}}, \\ t_{\text{edge}} &= d_{\text{edge}} / v_a, \\ \Delta t_{\text{coast}} &= d_{\text{coast}} / \sqrt{gh}, \end{aligned} \right\} \quad (\text{M15})$$

583 where  $d_{\text{edge}}$  is the distance between the eruption site and the excitation area's edge closest to the tsunami  
584 observation location,  $v_a$  is the traveling velocity of the atmospheric pressure wave, and  $d_{\text{coast}}$  is the distance  
585 between the edge and the tsunami observation location. For simplicity, the mean value of the still water depth  
586  $h$  was assumed as

$$h \simeq \begin{cases} 2000 \text{ m} & \text{in a deeper area, e.g., offshore from a shelf slope} \\ 100 \text{ m} & \text{in a shallower area, e.g., on a continental shelf.} \end{cases} \quad (\text{M16})$$

588 Conversely, the estimated arrival time  $t_{\text{air}}$  was evaluated by

$$t_{\text{air}} = (d_{\text{edge}} + d_{\text{coast}}) / v_a. \quad (\text{M17})$$

590 Tab. 2 lists the estimated arrival time  $t_{\text{tsunami}}$  at each tsunami observation location, and the obtained results  
591 of  $t_{\text{tsunami}}$  are shown in red. In the table, the estimated arrival time  $t_{\text{air}}$  for each traveling velocity of atmospheric  
592 pressure waves,  $v_a$ , is shown in blue. As indicated in Tab. 2, the time difference  $t_{\text{tsunami}} - t_{\text{air}}$  was in the range of  
593 10–50 min.

## 595 Acknowledgments

596 The atmospheric pressure data of Soratena were provided by Weathernews. The atmospheric pressure data  
597 were provided by Nakajo, S. of Osaka City University, with a grant of JSPS KAKENHI Grant Number  
598 JP20H02260. We used the worldwide tide-level data of Carvajal et al.<sup>2</sup> (<https://watershed.sdsu.edu/research>).  
599 The global bathymetric data were obtained from GEBCO (<https://www.gebco.net>). This work was supported  
600 by JSPS KAKENHI Grant, the Grant Numbers of which were JP17K06585 and JP21K21353.

## 602 Data availability

603 The numerical result data and used code in this study are available from the corresponding author on reasonable  
604 request.

## 606 Contributions

607 KY and TK designed the research, interpreted the obtained results, and wrote the manuscript collaboratively.  
608 KY developed the method and performed the numerical calculations.

## 610 Conflicts of Interest

611 The authors declare no conflicts of interest.

## 613 References

- 614 1. Study session on tsunami prediction technology. Report on tide level changes caused by Hunga Tonga-  
615 Hunga Ha'apai volcanic eruption, Japan Meteorological Agency, 33p., 2022.  
616 [https://www.data.jma.go.jp/eqev/data/study-panel/tsunami/tonga-houkokusho/houkoku\\_honbun.pdf](https://www.data.jma.go.jp/eqev/data/study-panel/tsunami/tonga-houkokusho/houkoku_honbun.pdf)  
617 (accessed on June 5, 2022). (In Japanese)
- 618 2. Carvajal, M., Sepúlveda, I., Gubler, A., and Garreaud, R. Worldwide signature of the 2022 Tonga volcanic  
619 tsunami. *Geophysical Research Letters* 2022, 49, e2022GL098153. doi: 10.1029/2022GL098153.
- 620 3. Harkrider, D. and Press, F. The Krakatoa air-sea waves: an example of pulse propagation in coupled  
621 systems. *Geophysical Journal International* 1967, 13, 149–159. doi: 10.1111/j.1365-246X.1967.tb02150.x.
- 622 4. Pelinovsky, E., Choi, B.H., Stromkov, A., Didenkulova, I., and Kim, H.-S. Analysis of tide-gauge records  
623 of the 1883 Krakatau Tsunami, In: Satake, K. (Ed.) *Tsunamis. Advances in Natural and Technological*  
624 *Hazards Research*, 23, Springer, Dordrecht. doi: 10.1007/1-4020-3331-1\_4, 2005.
- 625 5. Kubota, T., Saito, T., and Nishida, K. Global fast-traveling tsunamis driven by atmospheric Lamb waves  
626 on the 2022 Tonga eruption, *Science*, eabo4364, 2022. doi: 10.1126/science.abo4364.
- 627 6. Sekizawa, S. and Kohyama, T. Meteotsunami observed in Japan following the Hunga Tonga eruption in  
628 2022 investigated using a one-dimensional shallow-water model, 2022. doi: 10.31223/X5KS78. (Preprint)
- 629 7. Tanioka, Y., Yamanaka, Y., and Nakagaki, T. Characteristics of tsunamis observed in Japan due to the air  
630 wave from the 2022 Tonga eruption, *Earth, Planets and Space*, 74, 61, 2022. doi: 10.1186/s40623-022-  
631 01614-5.
- 632 8. Proudman, J. The effects on the sea of changes in atmospheric pressure. *Geophysical Journal International*  
633 1929, 2(s4), 197–209. doi: 10.1111/j.1365-246X.1929.tb05408.x.
- 634 9. Kataoka, R., Winn, S.D., and Touber, E. Meteotsunamis in Japan associated with the Tonga Eruption in  
635 January 2022, *SOLA*, 2022. <https://doi.org/10.2151/sola.2022-019>.
- 636 10. Ramírez-Herrera, M. T., Coca, O., and Vargas-Espinosa, V. Tsunami effects on the Coast of Mexico by the  
637 Hunga Tonga-Hunga Ha'apai volcano eruption, Tonga, *Pure and Applied Geophysics*, 179, 1117–1137,  
638 2022. doi: 10.1007/s00024-022-03017-9.
- 639 11. Garrett, C. J. R. A theory of the Krakatoa tide gauge disturbances. *Tellus*, 22, 43–52, 1970. doi:  
640 10.1111/j.2153-3490.1970.tb01935.x.
- 641 12. Kakinuma, T. Tsunamis generated and amplified by atmospheric pressure waves due to an eruption over  
642 seabed topography, *Geosciences*, 12, 232, 2022. doi: 10.3390/geosciences12060232.
- 643 13. UNESCO/IOC. Sea level station monitoring facility, 2022. <http://www.ioc-sealevelmonitoring.org/list.php>  
644 (accessed on June 5, 2022).
- 645 14. Amores, A., Monserrat, S., Marcos, M., Argüeso, D., Villalonga, J., Jordà, G., and Gomis, D. Numerical  
646 simulation of atmospheric Lamb waves generated by the 2022 Tonga volcanic eruption, *Geophysical*  
647 *Research Letters*, 49, 2022. doi: 10.1029/2022GL098240.
- 648 15. Burt S. Multiple airwaves crossing Britain and Ireland following the eruption of Hunga Tonga–Hunga  
649 Ha'apai on 15 January 2022, *Weather*, 77, 76–81, 2022. doi: <https://doi.org/10.1002/wea.4182>.
- 650 16. Kobayashi, T. and Kakinuma, T. Tsunamis propagated by airwaves generated by explosive volcanic

- eruptions: the 1883 Krakatau and the 1956 Bezymianny eruptions. Proceedings of the International Meeting on Eruptive History and Informatics, 2021-2, 93–105, 2022. (In Japanese)
17. Murayama, N. Propagation of atmospheric pressure waves produced by the explosion of volcano Bezymianny of March 30, 1956 and transport of the volcanic ashes, Quarterly Journal of Seismology, Vol.33, 1–11, 1969. [https://www.jstage.jst.go.jp/article/jmsj1923/40/4/40\\_4\\_222/](https://www.jstage.jst.go.jp/article/jmsj1923/40/4/40_4_222/) pdf. (In Japanese)
18. Koike, R. Microbarometric observations of the off Etorofu Island Earthquake on 7 Nov., 1958 and of the large explosion at Mt. Asama on 10 Nov., 1958, Quarterly Journal of Seismology, 24, 45–46, 1959. (In Japanese)
19. Tanaka Y. Propagation of the shock waves, produced by the explosion of the volcano, The Journal of the Acoustical Society of Japan, 40, 830–836, 1984. (In Japanese)
20. Tahira, M., Nomura, M., Sawada, Y., and Kamo, K. Infrasonic and Acoustic-Gravity Waves Generated by the Mount Pinatubo Eruption of June 15, 1991, C.G. Newhall, R.S. Punongbayan (Eds.), Fire and Mud, University of Washington Press, Seattle, pp. 601–614, 1996.
21. Soloviev, S.L. Basic data of tsunamis in the Pacific coast of USSR, 1937–1976, In A Study of Tsunamis in the Open Sea, Academii Nauk, Moscow, 61–136, 1978. (In Russian)
22. Witze, A. Why the Tongan eruption will go down in the history of volcanology, Nature, 602, 376–378, 2022. doi: 10.1038/d41586-022-00394-y.
23. Cas, R.A.F. and Simmons, J.M. Why deep-water eruptions are so different from subaerial eruptions, Frontiers in Earth Science, 20, 2018. doi: 10.3389/feart.2018.00198.
24. Manga, M., Fauria, K.E., Lin, C., Mitchell, S.J., Jones, M., Conway, C.E., Degruyter, W., Hosseini, B., Carey, R., Cahalan, R., Houghton, B.F., White, J.D.L., Jutzeler, M., Soule, S.A., and Tani, K. The pumice raft-forming 2012 Havre submarine eruption was effusive, Earth and Planetary Science Letters, 489, 49–58, 2018. doi: 10.1016/j.epsl.2018.02.025.
25. Yuen, D.A., Scruggs, M.A., Spera, F.J., Zheng, Y., Hu, H., McNutt, S.R., Thompson, G., Mandli, K., Keller, B.R., Wei, S.S., Peng, Z., Zhou, Z., Mulargia, F., and Tanioka, Y. Under the surface: pressure-induced planetary-scale waves, volcanic lightning, and gaseous clouds caused by the submarine eruption of Hunga Tonga-Hunga Ha’apai volcano provide an excellent research opportunity, Earthquake Research Avances, 2022. doi: 10.1016/j.eqrea.2022.100134.
26. Iwase, H., Mikami, T., and Goto, C., Practical tsunami numerical simulation model by use of non-linear dispersive long wave theory, J. JSCE, 600/II-44, 119–124, 1998. doi: 10.2208/jscej.1998.600\_119. (In Japanese)
27. Peregrine, D.H., Long waves on a beach, Journal of Fluid Mechanics, 27, 815–827, 1967. doi: 10.1017/S0022112067002605.
28. Baba, T., Allgeyer, S., Hossen, J., Cummins, P. R., Tsushima, H., Imai, K., Yamashita, K., and Kato, K. Accurate numerical simulation of the far-field tsunami caused by the 2011 Tohoku earthquake, including the effects of Boussinesq dispersion, seawater density stratification, elastic loading, and gravitational potential change, Ocean Modelling, 111, 46–54, 2017. doi: 10.1016/j.ocemod.2017.01.002.